Convection and Crystallization in a Liquid Cooled from above: an Experimental and Theoretical Study

Article *in* Journal of Petrology · August 1999

DOI: 10.1093/petrology/40.8.1271

4 authors, including:

Bruce D. Marsh
Johns Hopkins University
178 PUBLICATIONS **7,043** CITATIONS
SEE PROFILE

Ronald G. Resmini
L3Harris Corporation
50 PUBLICATIONS **373** CITATIONS
SEE PROFILE

JOURNAL OF PETROLOGY | VOLUME 40 | NUMBER 8 | PAGES 1271–1300 | 1999

Convection and Crystallization in a Liquid Cooled from above: an Experimental and Theoretical Study

M. HORT[1]*, B. D. MARSH[2], R. G. RESMINI[2]† AND M. K. SMITH[3]

[1]GEOMAR, VULKANOLOGIE UND PETROLOGIE, WISCHHOFSTR. 13, D-24148 KIEL, GERMANY

[2]MORTON K. BLAUSTEIN DEPARTMENT OF EARTH AND PLANETARY SCIENCES, JOHNS HOPKINS UNIVERSITY, BALTIMORE, MD 21218, USA

[3]GEORGIA INSTITUTE OF TECHNOLOGY, WOODRUFF SCHOOL OF MECHANICAL ENGINEERING, ATLANTA, GA 30332, USA

RECEIVED SEPTEMBER 30, 1998; REVISED TYPESCRIPT ACCEPTED FEBRUARY 23, 1999

Evidence from experiments and theoretical modeling suggests that systems crystallizing exclusively from the top down and rejecting a buoyant liquid effectively cease convecting once the initial superheat has been lost. We report here on a combined experimental and theoretical study designed to investigate in some detail the interaction of convection and crystallization in a fluid cooled from above. The experiments are carried out in a small tank where temperature, composition, mush thickness, and convective velocities have been monitored. After an initial period of turbulent convection removing the superheat, the bulk fluid temperature holds steady at the liquidus temperature. Further convection at $Ra \sim 10^6$ *is characterized by a gentle, broad stirring of the entire tank through upward boundary layer flows hugging the tank walls, which are inferred to be sustained by a small but steady leakage of heat into the tank through the sidewalls. The thickness of the overlying mush zone increases linearly with* $\sqrt{t}$ *and is found to be very sensitive to leakage of heat through the sidewalls. Within the uncertainty of the liquidus determination, there is no measurable undercooling and no crystallization is observed within the bulk fluid. The experimental results are investigated with a comprehensive analytical model employing sidewall heating and, among other things, either equilibrium or disequilibrium crystallization. Either crystallization model gives satisfactory agreement with the experiments. More importantly, however, once the superheat is lost all the convective motion is well explained by the unwanted sidewall heating, and if this heat source is then 'analytically' turned off, convection ceases upon loss of the superheat. In sum, this combined study supports the conclusion that convection in similar binary phase systems crystallizing from the top down and rejecting a buoyant liquid becomes non-turbulent or even ceases upon loss of the superheat. Transferring these results to magmatic systems, we suggest that the dynamics inside intrusive bodies upon cooling are very sensitive to the actual phase diagram, the kinetics of crystallization and the density relation between crystals and melt.*

KEY WORDS: *magma physics; convection; solidification; crystallization; experiment*

INTRODUCTION

The question of the nature of convection during solidification is central to understanding the dynamics of any crystallizing fluid (Davis, 1992; Beckermann & Viskanta, 1993), but the case of magma is especially peculiar (Bergantz, 1992). Convection in magma, if present, may play a central role in the nucleation, growth, sorting, and redistribution of crystals, which may foster extensive chemical differentiation and varied layering seen in some magmatic rocks (e.g. Sparks & Huppert, 1987; Parsons, 1987; Worster *et al.*, 1990, 1993; Jaupart & Tait, 1995). That crystal layering is often due to sedimentation in moving magma is clear (e.g. Irvine, 1980), but it is much less clear if this motion is due to thermal convection,

*Corresponding author. GEOMAR, Vulkanologie und Petrologie, Wischhofstr. 13, D-24148 Kiel, Germany. Tel.: 49 431 600 2645. Fax: 49 431 600 2978. e-mail: mhort@geomar.de

†Present address: SAIC, 4501 Daly Drive, Suite 400, Chantilly, VA 20151, USA.

compositional convection, crystal sedimentation, or some combination of these. The possibility of compositional convection (e.g. Tait & Jaupart, 1992*a*) reflects one of the most important characteristics of magma, namely, that it is a multicomponent system solidifying over a wide range of temperatures, typically 150–250°C. Within this solidification interval or front the overall viscosity increases dramatically with increasing crystallinity until near a crystal content of ~55% the effective viscosity becomes enormous (e.g. Marsh, 1981; Ryerson *et al.*, 1988; Lejeune & Richet, 1995). Philpotts & Carroll (1996) described even for a crystallinity as low as 30% a relatively strong network of crystals resisting large compressive strengths. A similar network has also been described by Marsh (1996) for crystallinities as low as 10%. The presence, position, and thermal and chemical behavior of such solidification fronts and networks of crystals are crucial to understanding magmatic evolution.

Size and shape of magmatic intrusions are variable and extend from vertical dike-like intrusions (e.g. sheeted dikes in the oceanic crust) to bodies of nearly cubic shape [e.g. magma storage beneath Kilauea volcano, Ryan *et al.* (1981)] and further to sill-like intrusions spreading horizontally in the Earth's crust (e.g. Mangan *et al.*, 1993). It seems that there is no real shape preference, and our knowledge of intrusive bodies is strongly biased towards exhumed bodies. Depending on the shape of the intrusion, cooling conditions are variable, with most heat loss through the sides in the case of dike-like intrusions (top and bottom cooling can be neglected) and strong top and bottom cooling in the case of sheet- or sill-like intrusions, where heat loss through the sides of the system is relatively unimportant; the latter form of intrusions is of interest to this study.

In the case of horizontal sheet-like structures cooling from below the system is generally thermally stable but could give rise to compositional convection (e.g. Tait & Jaupart, 1992*a*: Hellawell *et al.*, 1993; Jaupart & Tait, 1995). For horizontal sheet-like systems cooled from above the situation is not as straightforward: compositional as well as thermal effects may lead to instability and convection. Most of the negative buoyancy generated in cooling and crystallization at the top is locked within the high-viscosity, inward moving solidification fronts, and is not available to drive convection (e.g. Smith, 1988; Marsh, 1989; Jaupart & Tait, 1995) (see Fig. 1). In fluids possessing a viscosity highly sensitive to temperature, but free of crystallization, the high-viscosity lid has a strong effect on convection [Richter *et al.*, 1983; Smith, 1988: Davaille & Jaupart, 1993*b*; and Solomatov (1995) for an excellent review]. On this basis and because of the great facility of high Rayleigh number (Ra) convection for cooling, Marsh (1989) suggested that once the superheat is removed the thermal Ra in a system solidifying by cooling from above is buffered at relatively low values

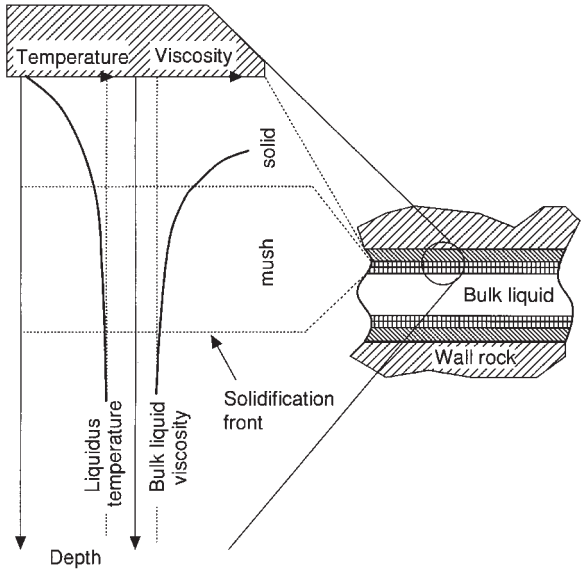

Fig. 1. Schematic drawing of a cooling layer of magma (i.e. in a sheet-like intrusion) showing the upper and lower (for cooling from the bottom) crust. Most of the negative buoyancy available to drive convection is locked up in the solid or mush and is too rigid to participate in the flow. The central region of the intrusion is close to or at its liquidus temperature. Redrawn and simplified after Marsh (1989) (his fig. 8).

and convection is non-turbulent. This speculation has stirred some debate on the magnitude of the Ra governing convection in magmas solidifying from above (see Huppert & Turner, 1991; Marsh, 1991). At least in the case of magma there appears to be no simple solution to this debate as magma is a multicomponent system and, depending on the initial melt composition, the crystallization sequence may vary greatly. This sequence controls the liquidus phase (e.g. olivine, pyroxene, plagioclase) and the temporal evolution of the density of the residual fluid, and the viscosity of the system. The chemically complex, multiply saturated nature of silicate melts makes it therefore difficult to generalize results; this has been emphasized by Bennon & Incropera (1987) and demonstrated in numerical experiments by Oldenburg & Spera (1992).

A unique solution to the problem of convection and crystallization in magmatic systems does not exist and a careful consideration of every case is necessary. It is therefore useful experimentally to investigate chemically analogous systems to elucidate some of the fundamental controls on convection and crystallization. Because an analog fluid possessing all properties of a magma has yet to be identified, each experiment can only be extrapolated to magmatic systems by carefully comparing the phase relations, viscosity and crystallization sequence. Typically, it is one or two key magmatic processes that experiments are specifically designed to study and from which the detailed dynamic evolution of a group of magmas is

deduced. As insight into key magmatic processes ultimately rests on evidence from the rock record, it is essential that this evidence and the uncertainties in interpreting the rocks themselves be appreciated. We begin below with an appraisal of the geologic evidence relative to the application of experiments on analog systems, then describe the layout of the remainder of the paper.

GEOLOGIC EVIDENCE AND LABORATORY EXPERIMENTS

Although it has long been held that many large (i.e. 500 km^3) magmatic intrusions show strong vertical compositional variations attributable to crystal fractionation by settling, it has become increasingly clear that the dynamic history of these bodies is by no means unequivocal enough to allow any concise quantitative identification of the key magmatic processes (e.g. McBirney, 1995). The image of an instantaneously injected vat of an initially crystal-free and well-mixed magma that subsequently grows crystals throughout, which settle and chemically differentiate the magma, is being replaced by a magma chamber formed by repeated inputs of often crystal-laden suspensions and crystallizing from the margins inward (e.g. Gibb & Henderson, 1992; Sorensen & Wilson, 1995). The most effective crystal settling involves crystals grown elsewhere—so-called phenocrysts—and injected with the magma itself (Marsh, 1996). These crystals settle to form thick mush piles on the floor in addition to the mush growing from below because of cooling, within which the interstitial melt may become chemically modified and migrate, as in compositional convection, to other areas of the body (Tait & Jaupart, 1992*b*; McBirney, 1995: Jahrling, 1997). The principal effects of differentiation are due to the injected phenocrysts and bottom crystallization, not new crystals grown in the interior or at the margins, which are probably trapped within the inward advancing solidification fronts (Mangan & Marsh, 1992). Depending on the actual phases precipitating and the density of the residual melt the possibility of the crystal-laden plumes leaving the upper solidification front has, however, been discussed (Brandeis & Jaupart, 1986; Simakin *et al.*, 1997).

The ineffectiveness of differentiation as a result of crystals grown *in situ* is dramatically displayed in smaller sheet-like magmas, or sills, of which there are literally hundreds throughout the world, ranging in thickness from 1 to 1000 m and in length from 1 to 100 km or more. Because of their relative simplicity of formation and expansiveness, these bodies are particularly attractive for identifying some key processes attending solidification. Broadly speaking, these bodies are of two basic types: (1) those formed of magma initially free of crystals or phenocrysts; (2) those formed of one or more injections of phenocryst-laden magma. The type (1) sills, of which the 330 m × 50 km Peneplain Sill of Antarctica is a good example (Marsh, 1996), are of a nearly uniform composition, showing no sign of differentiation. The type (2) sills, of which the 100 m × 20 km Namibian sill is a good example (Richardson, 1979), show gradational variations from the most differentiated magma at the margins to the least differentiated magma at the center; exactly the opposite of that expected from progressive inward crystallization. This inverted compositional variation is generally recognized to represent emplacement of crystal-laden magma that has become flow differentiated during ascent (e.g. Upton & Wadsworth, 1967; Gibb, 1968; Richardson, 1979). In response to the effects of drag in a shear flow, heavy crystals in an ascending fissure of magma migrate downward and inward, producing a differentiated column of magma (e.g. Segre & Silberberg, 1962; Leal, 1980; Marsh, 1996). The leading region, having lost its crystals, is most differentiated and goes to form the margins of the sill, whereas the crystal-laden magma arrives later and fills the center of the sill. That there is evidently no thorough homogenization of the magma subsequent to emplacement can be interpreted as a lack of thermal or compositional convection or perhaps discontinuous or sequential injection (Gibb & Henderson, 1992).

The evidence from phenocryst-free sills suggests that either (1) convection is so vigorous in the sill interior that newly grown crystals are never able to settle and differentiate the magma, or (2) convection is weak and crystal growth is essentially confined to the solidification fronts, which easily capture crystals and stifle differentiation. In the phenocryst-rich sills, either (1) crystals are not redistributed by convection, or (2) emplacement is slow and in pace with solidification itself, which precludes both convection and crystal settling. These key processes cannot be easily identified and modeled without some clear insight into how simple systems evolve during crystallization from the top down.

Given the magmatic conditions outlined above and the fact that only one or two processes related to magma can be studied in analog experiments, we focus on thermal convection in a fluid layer being cooled from above and not crystallizing in the interior, a situation which may be met in at least the upper half of sills (see also Fig. 1). Similar crystallization experiments involving thermal convection as a result of cooling from above have been carried out by Kerr *et al.* (1989, 1990*a*, 1990*b*, 1990*c*) and Brandeis & Marsh (1989, 1990), and more recently by Wettlaufer *et al.* (1997). In a nutshell, Kerr *et al.* interpreted their experimental results from crystallizing separate aqueous solutions of isopropanol (Kerr *et al.*, 1989, 1990*a*, 1990*b*) and Na_2SO_4 (Kerr *et al.*, 1990*c*) as a reflection of turbulent thermal convection in the underlying uncrystallized liquid during most of the

solidification process, whereas Brandeis & Marsh (1989, 1990) in a broadly similar set of experiments using paraffin as a fluid observed a rapid and dramatic cessation of thermal convection as the initial superheat was evicted from the system. Furthermore, in contrast to the findings of Kerr *et al.* (1990*b*), Brandeis & Marsh (1989, 1990) did not observe any undercooling or internal crystallization in the bulk liquid. The contradictory findings of these two studies suggest that chemically different systems may behave dynamically differently when cooled from above, making it difficult to generalize results, a conclusion stressed above.

In this study we set out to investigate in some detail the thermal, compositional and dynamic evolution in a system cooled from above and releasing a buoyant liquid upon crystallization, i.e. a chemically distinct system which can be considered as one end-member of a magmatic system. We investigate in some detail the boundary layer associated with the solidification process, as it is in this part of the system that negative buoyancy is generated to drive thermal convection and therefore is the key process controlling the thermal evolution in this type of system. We begin with a description of the experimental setup and the specific techniques used to examine the thermal and compositional evolution of the melt. This is followed by a presentation of the experimental results, which are then compared with results predicted by the model calculations, including the effect of a sidewall heat flux. A comparison of our results with earlier studies of systems cooled from above follows. Here we offer among other things an alternative interpretation of the experimental results of Kerr *et al.* (1990*a*, 1990*b*). We finish with a concluding discussion of some of the implications of this study for understanding convection in magmatic systems.

EXPERIMENTAL SETUP

The experiments are carried out in a 20·2 cm × 20·2 cm × 20·2 cm Plexiglas tank with 1·85 cm thick walls and bottom. The top of the tank is a brass plate in which a water–methanol mixture circulates under thermostatic temperature control. The tank is filled with a water–isopropanol solution containing 16·8 wt % isopropanol. We used 'Baker analyzed' Reagent 2–propanol and distilled water for preparing the mixture. The great advantage of this composition, as pointed out by Kerr *et al.* (1990*a*), is that when cooled below its liquidus temperature the rejected residual fluid is buoyant. When the tank is cooled from above, compositional convection therefore does not occur. Moreover, the anomalous density maximum at 4°C associated with pure water disappears for an alcohol content larger than ~12 wt %. The tank itself is packed in 3·8 cm thick closed cell foam thermal insulation with a thermal conductivity of $k_f = 0{\cdot}039$ W/m per °C at 20°C. In addition, the entire tank with its insulation resides in a refrigerator maintained at ~0°C. A fan installed within the refrigerator maintains a constant temperature throughout the refrigerator and guarantees air circulation. The effectiveness of the insulation was tested by maintaining a constant temperature of –6°C at the top brass plate and measuring the long-term temperature inside the tank. The average temperature in the tank of fluid holds steady after 15 h at –5·55°C, which indicates a small unwanted heat flux into the system (this is considered further below).

Temperatures inside the tank are monitored by nine vertically spaced and four horizontally spaced K type thermocouples (see Fig. 2). A 16 bit A/D converter (Omega WW-AAI-B16) records the voltages of the thermocouples, which are converted to temperatures through calibration curves. The voltages are measured against a reference thermocouple placed in an ice bath maintained at 0°C. The uncertainty of the temperature readings is about $\pm 0{\cdot}07$°C above –7·5°C and $\pm 0{\cdot}1$°C below –7·5°C. In addition to the temperatures in the tank we also monitor the temperature of the cooling plate and that of the refrigerator in which the complete tank assembly is installed. Temperatures are recorded every 60 s. To monitor the composition of the liquid within the tank, five fluid taps are located inside the tank (see Fig. 2), which directly sample liquid throughout the tank. As the taps are tiny they do not affect the overall flow field. Between 1 and 1·5 ml of liquid is extracted through a syringe-like tapping during sampling, which means we sample a small but finite region around each tap orifice. The composition of the liquid is determined with a thermostatted refractometer and a calibration curve relating the index of refraction to wt % alcohol in the fluid. The uncertainty of these measurements is about $\pm 0{\cdot}1$ wt %. The fluid in the tank is periodically sampled and the growth of the crust is continuously monitored by visual observation and direct measurement.

The mean convective velocity of the fluid was determined at different times in nine separate experiments by adding to the liquid a very small amount of tiny aluminum filings; otherwise, the experimental setup is as described. At a specific instant in an experiment, the usual insulation surrounding the tank was removed and the fillings were intermittently illuminated by a vertical ~1 cm thick sheet of light projected into the tank 6 cm from and parallel to one of the walls. After taking a long-exposure photograph, using exposure times between 5 and 25 s, the experiment was terminated. To characterize the convective motion quantitatively, we superimposed a grid of 42 squares over each image and measured the longest streak in each square. We converted streak lengths to velocities and calculated mean velocities.

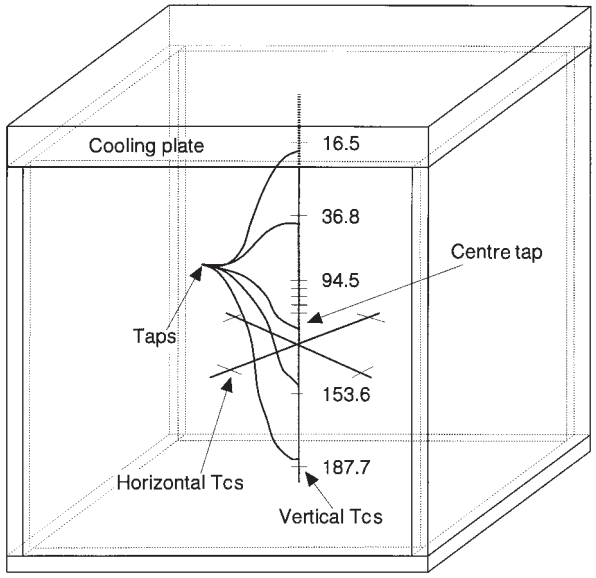

Fig. 2. Schematic drawing of the tank used in the experiments, showing the locations of the thermocouples and the taps used to measure temperatures and to sample the liquid during the experiment. The locations of the five center thermocouples from top down are: 94·5, 96·7, 98·7, 100·8, and 102·7 mm. All other distances given in the figure are also in mm.

To assess the importance of the small unwanted sidewall heat flux on the experimental results, a couple of experiments were made with the refrigerator held at –5°C instead of 0°C. In actual practice, however, the refrigerator temperature fluctuated between –4 and –5°C, and the boundary temperature is therefore assumed to be –4·5°C. Because measurements of the crust thickness entail actually opening the door of the refrigerator, too many measurements severely influence the repeatability of this type of experiment, and therefore these data are more sparse than for the usual 0°C runs. This was no problem in the case of the 0°C runs, as the refrigerator cooling was much more efficient and opening the refrigerator regularly did not interfere with the temperature measurements. In discussing the experimental results, we will always refer to the experiments conducted with a 0°C boundary condition; but where appropriate we also give data for the experiments at the –4·5°C boundary temperature.

Each experiment began with the fluid in the tank being homogenized through circulation with a pump for 10–15 min. This was found to be necessary as some stratification of the fluid inside the tank after thawing the solution from a previous run was commonly observed. The initial temperature of the water–isopropanol mixture in the tank was ~0–0·1°C, and to insure homogeneity the liquid was sampled and its composition determined at five locations (see Fig. 2). The cooling fluid was next pumped through the top plate: its temperature increased over the first 25 min from initially about –30°C to about –21°C, and henceforth a constant temperature of –20°C was established throughout the rest of the experiment. Expansion and contraction of the fluid was accommodated through an overflow.

Overall, the general experimental setup is similar to that of other experiments where liquids have been cooled from above to study thermal convection. A new feature in our experiments is the simultaneous monitoring of composition and temperature for this type of system, as well as the determination of the unwanted sidewall heat flux occurring during the experiment and measurements of mean convective velocities. Kerr *et al.* (1989, 1990*a*), who also worked with a water–isopropanol solution of similar composition in a similar setup, had slightly different initial and boundary conditions during their experiments. Our initial temperature was lower (0°C vs 4°C) and the cooling plate was held at a higher temperature (–20°C vs –25°C). The higher cooling plate temperature helped avoid the possible two-liquid region (below –20°C) in the phase diagram, as determined by Rosso & Carbonnel (1969). The reduced initial temperature was chosen to reduce slightly the initial amount of superheat in the system, which simply allows for shorter overall run times. Altogether we performed some 78 experiments on this system.

RESULTS

We begin with the phase diagram of the water–isopropanol solution used as the working fluid throughout this study. This is followed by a presentation of the general evolution of the vertical and horizontal temperature structure throughout the tank as a function of time. Next, we tie the measurements of crust growth to the temperature field, which allows an estimate of the temperature at the leading edge of the crystallization front. This temperature is then compared with both the observed and equilibrium liquid compositions in the vicinity of the leading crust–liquid or crystal interface. We close this section by presenting measurements of the convective velocities.

The liquidus temperature

Water and isopropanol form a binary eutectic over a temperature range from 0°C to approximately –100°C (Rosso & Carbonnel, 1969; Ott *et al.*, 1979; J. B. Ott, personal communication, 1992) with the eutectic lying far to the isopropanol side of the binary. The compositional region of interest to the present study is a very restricted, water-rich composition containing a mole fraction of water of ~0·943 or 16·8 wt % isopropanol. Although data for the full system have been provided only by

Rosso & Carbonnel (1969) and Ott *et al.* (1979), the water-rich end of the system has also been investigated by Abegg (1894) and Lange (1967). The data of Ott *et al.* (1979) and Rosso & Carbonnel (1969) give almost the same values for the liquidus (between –6·9 and –7·0°C) in the region of interest, the data of Abegg (1894) lie about 0·7°C above those data, and Lange's data are about 1·6°C below the values of Ott *et al.* (1979) and Rosso & Carbonnel (1969) (for details on the data and techniques used by the different researchers, see the Appendix). Our own data (a total of 70 measurements; for details see also the Appendix) confirm the measurements of Ott *et al.* (1979) as well as Rosso & Carbonnel (1969), resulting in a liquidus temperature of –6·95°C ± 0·1°C for the solution used during the experiments.

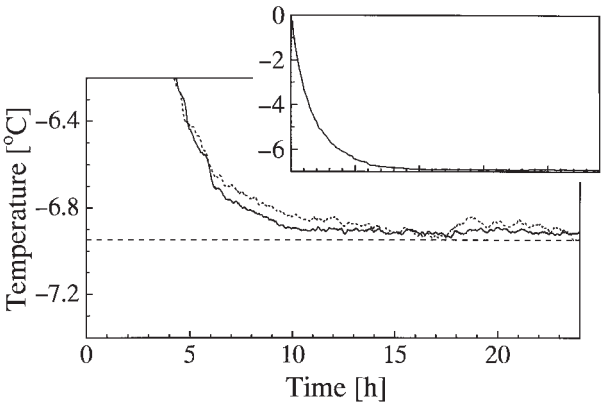

Fig. 3. Temperature of the residual liquid underlying the mush as a function of time. The *y*-axis on the inset is temperature and shown is the thermal evolution at the lowermost thermocouple. The continuous line in the main part of the figure again shows the temperature at the bottom thermocouple (188 mm from the top); the dashed line shows that at 154 mm from the top. In this figure the temperature has been averaged over an 11 min interval for clarity. The true resolution of our temperature measurement can be seen in, e.g. Fig. 4.

Temperature evolution as a function of time

Vertical temperature structure

The temperature in the liquid as a function of time at the two lowest locations of the tank (see Fig. 2) is shown in Fig. 3. The two curves shown in this figure summarize some of the most important characteristics of the experiments:

(1) early in the experiment the temperature drops rapidly because of the removal of the superheat from the system.

(2) After about 8–10 h the temperature levels out and remains constant near –6·9°C. When the external wall temperature is –4·5°C, this 'leveling' temperature drops between –7·0 and –7·1°C (not shown). We expect this temperature to be closer to the temperature the system would reach if it were perfectly insulated. The difference between these two temperature measurements appears to be significant and is explained by the analytical model presented below. In passing, it is also important to mention that the composition of the bulk liquid underlying the crystallization front, as measured with tapping, does not change with time. This shows that even at late times in the experiment (>10 h), when the superheat is gone, there is no crystallization in the bulk liquid, nor is there any detectable mixing of alcohol-enriched fluid with the bulk liquid, i.e. the bulk liquid composition does not change measurably during the entire experiment.

(3) In the late stages of the experiment, after about 24 h, the temperature of the upper thermocouple (dashed line in Fig. 3) approaches the liquidus (straight dashed line in Fig. 3), as the downward growing mush starts to approach this thermocouple (see also below).

(4) Comparing the readings of the two thermocouples in the lower part of the tank, one finds the difference between the two recorded temperatures to be well within the uncertainty of the measurements themselves. This means that once the system becomes well mixed it remains so; there is no thermal stratification in the fluid. This was verified by interchanging the two lowermost thermocouples to exclude a calibration error.

Some of these features were also described by Kerr *et al.* (1989, 1990*a*) and similar observations were made by Brandeis & Marsh (1989, 1990) in their experiments involving paraffin.

Horizontal temperature structure

The temperature as a function of time for two of the four thermocouples mounted in the horizontal plane at a depth of 120 mm is shown in Fig. 4. The general temporal evolution of the temperature is as described above. Again, the temperature first drops quickly and then levels out at about –6·9°C. It starts dropping again, as the mush approaches the thermocouples, although the drop occurs earlier than in Fig. 3, because these thermocouples are positioned higher in the tank (see Fig. 2).

With the four thermocouples mounted in a horizontal plane, a subtraction of measurements from one another provides six independent temperature differences between the four thermocouples, which can be used as a measure of the horizontal thermal structure of the fluid. The temperature differences, for example, between the two curves given in Fig. 4 are shown in Fig. 5. During the early stages of the experiment (<4 h) these differences are rather large (~ ± 0·3°C), and clearly reflect turbulent convective motion during removal of the initial superheat from the system leading to larger local differences in temperature as a result of cold plumes separating and

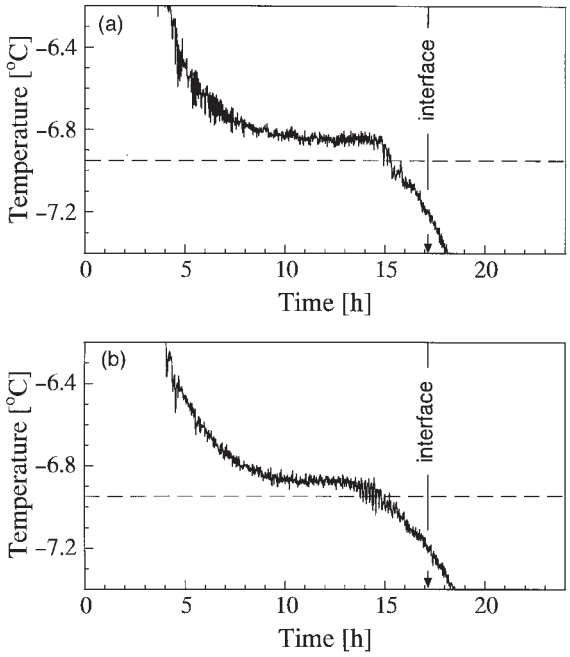

Fig. 4. Temperatures from two of the four thermocouples mounted in the horizontal plane (see Fig. 2). The arrows indicate the time when the crust overtakes the thermocouples. These times were calculated using the 0°C crust growth law derived from the data presented in Fig. 6.

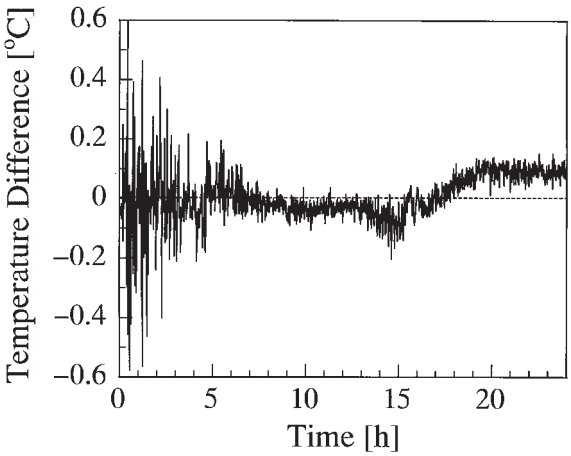

Fig. 5. Temperature difference between the two data sets given in Fig. 4.

dropping from the cooled top of the tank and sinking into the tank. After about 7 h the temperature differences become rather small and in this case are slightly negative. Once overtaken by the mush at about 17 h the difference becomes positive, which may reflect some distortion of the array by the growing mush or a small positioning error of the individual thermocouples in the array. Similar observations are made for the other five differences. To exclude the possibility that this observation is a function of the exact location of the thermocouples in the horizontal plane, we used three different thermocouple setups and always found the same general behavior. These data suggest that convection in the first 7 h is dominated by turbulent convection with cold plumes dropping from the mush interface. After 7 h, when most of the superheat has been removed from the system (see also Fig. 3), there are no longer large cold plumes sinking towards the bottom of the tank and motion in the system is dominated by a broad, gentle cellular circulation (see also below). This general behavior described above is independent of the wall boundary condition (i.e. 0°C vs –4·5°C).

Growth of the mush

Detection of the mush front

Before discussing the mush thickness measurements in detail, it is important to consider what thickness is actually determined by visual observations. Monitoring an interface during the solidification of a one-component system is fairly easy, because at the solidification front the liquid is completely transformed into a solid. Monitoring the solidification front in a multicomponent system, however, depends on observing the first appearance of nuclei, which is virtually impossible. There must always exist a finite amount of crystallization before a change in the opacity of the liquid is visible to the human eye. For the water–alcohol system this is further complicated by the precipitating phase (ice), which is nearly as transparent as the liquid itself. Furthermore, as crystal growth in this type of system under fairly rapid cooling conditions is dendritic, the number of dendrites per cm^2 of liquid can be estimated as a function of the degree of crystallization. Assuming, for example, a dendrite diameter of 0·5 mm, there is about one dendrite per cm^2 at a temperature of –6·97°C, and about 10 at –7·13°C. Being close to the liquidus it is therefore very difficult visually to detect the actual edge of the solidification front, but instead we see some slightly later stage where a significant visual difference is detected. The measurements of the mush thickness discussed henceforth thus pertain to the easily visible part of the mush, which is a very high fraction of the total actual thickness. Other techniques (e.g. Schlieren or shadow technique), which would resolve this interface much better, could not be employed because of the setup of the experiment in a refrigerator, which was necessary for the reduction of the external heat flow. The mush thickness was always determined in the center of the tank and at the end of some runs a very small curvature of the interface could be observed, which is attributed to the unwanted sidewall heat flux (see below).

Mush thickness with time

The evolution of the mush thickness as a function of time is shown in Fig. 6. Most of the data (134 meas-

urements) are from experiments with the 0°C wall temperature or boundary condition, although some data (23 measurements) are also shown for experiments under the –4·5°C boundary condition. These data clearly indicate that the boundary condition significantly influences the rate of growth of the mush zone. Any serious modeling attempt has to account for this observation. Beyond run times of 7 h, after which most of the superheat has been removed from the residual liquid (see Fig. 3), all the data vary linearly with $\sqrt{t}$ and can be fitted with linear equations (e.g. $h \propto \sqrt{t}$). These data follow the linear model within an accuracy of approximately $\pm$1·5–2 mm; $h = (-29{\cdot}961 \pm 0{\cdot}934) + (0{\cdot}599 \pm 0{\cdot}47 \times 10^{-2}) \times \sqrt{t}$ for the 0°C experiments, and $h = (-37{\cdot}158 \pm 2{\cdot}372) + (0{\cdot}680 \pm 0{\cdot}12 \times 10^{-1}) \times \sqrt{t}$ for the –4·5°C experiments, where t is in s and h is in mm. The uncertainty of our crust thickness measurement (early on ~1 mm; after 20 h ~4 mm) is included in the linear regression. The errors in the two fits are indicated by the dashed lines in Fig. 6. The higher uncertainty of coefficients in the linear model in the –4·5°C data reflects the relatively small data set (23 vs 134 measurements) on which this model is based.

The times when the mush–liquid interface reaches the individual thermocouples are noted on the temperature histories of Fig. 4. The temperature at this time is apparently slightly lower (~0·2°C) than the liquidus temperature of the solution itself. This difference is important to quantify, as it is crucial to understanding the overall dynamics of the system. Using the temperature readings of the five thermocouples mounted close together in the center of the tank and of the four thermocouples mounted in the horizontal plane (see Fig. 2 for location of the thermocouples), and employing the empirical mush growth law for the 0°C experiment, the average temperature at the liquid–mush interface is $-7{\cdot}22 \pm 0{\cdot}13$°C for $t > 11$ h. This value is based on 11 separate experiments involving 99 data points. The uncertainty of this value is determined from the uncertainty in the growth equation (see dashed lines in Fig. 6). However, even considering this uncertainty, the interface temperatures are still slightly lower than the liquidus temperature ($-6{\cdot}95 \pm 0{\cdot}1$°C) of the solution.

There are three possible explanations for this behavior:

(1) the alcohol content in the vicinity of the mush–liquid interface is higher and therefore the liquidus temperature is depressed. This is equivalent to the earlier statement that we are visually detecting the solidification front only at a slightly advanced degree of crystallization. Alternatively, diffusion and mechanical expulsion of isopropanol from the mush, because of expansion of the precipitated ice, increases the alcohol content in a thin layer ahead of the mush–melt interface.

(2) There is a thermal boundary layer preceding the crystallization front [a common observation in similar experiments, e.g. Huppert & Worster (1985) and Tait & Jaupart (1992*a*)], which accompanies a significant undercooling at the leading edge of the mush. This, however, requires no change in alcohol content in this layer.

(3) a combination of (1) and (2).

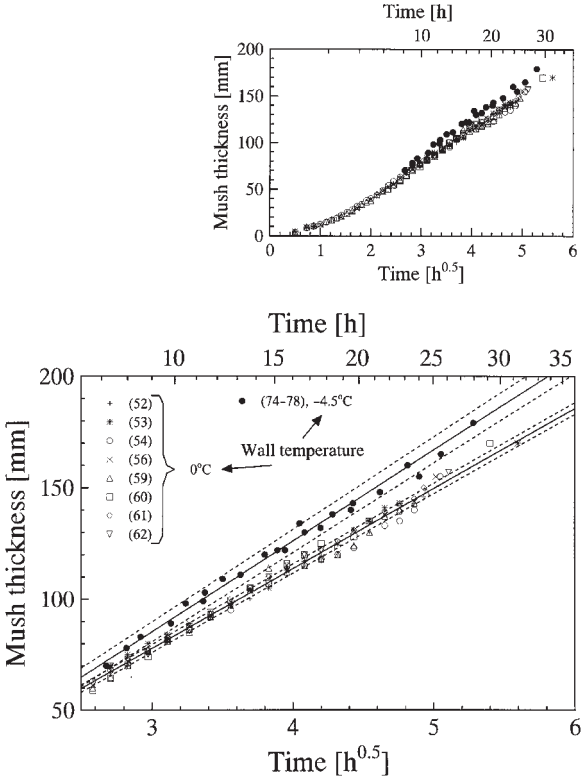

Fig. 6. Crust thickness as a function of the square root of time. The lower figure shows detail for 6·25–36 h. The various symbols indicate from which experiment the data were gathered. Experiment numbers 62 and below were carried out with the 0°C boundary temperature (open symbols); experiments 74 and above represent measurements during experiments with a –4·5°C boundary temperature (filled symbols). The dashed lines indicate the uncertainty in the mush thickness of the linear models used to fit the two data sets. For the 0°C boundary condition, the uncertainty of mush thickness is approximately $\pm$1·5–2 mm. For the –4·5°C boundary condition experiments the uncertainty is significantly larger, as the number of measurements on which the model is based is smaller.

The increase in alcohol content of the liquid, determined as a function of time from the index of refraction of the samples taken from the center tap (for location see Fig. 2) is shown in Fig. 7a. The data show a certain amount of scatter, which is inherent in the sampling method (see above). Nevertheless, there is a clear increase in alcohol content after about 13 h 20 min. At this time the visually detected mush–melt interface is located at 101·5 mm, which is ~5 mm above the location of the center tap. When the visually detected mush–melt interface finally reaches the center tap itself after 14 h

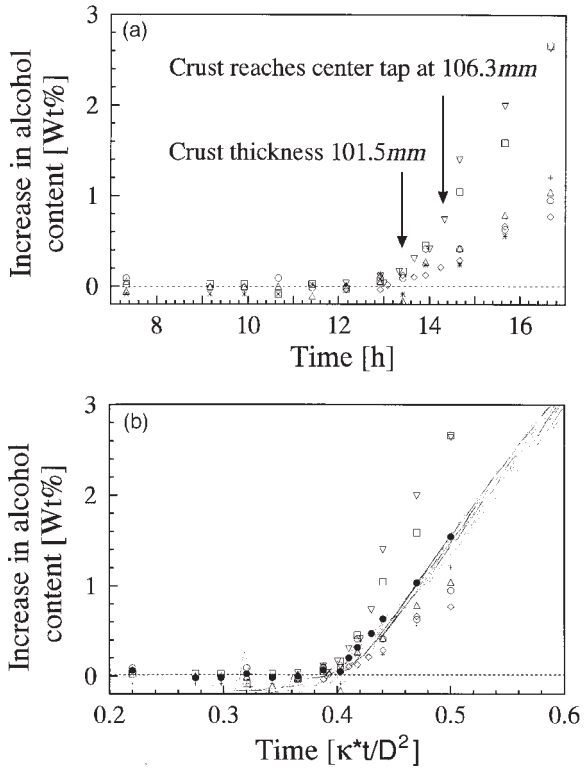

Fig. 7. (a) Increase in alcohol content relative to the alcohol content of the remaining liquid underlying the mush as a function of time at the center tap in the tank. (For the location of the tap, see Fig. 2.) The symbols refer to different experiments and are explained in Fig. 6. (b) Comparison of the compositional changes (symbols) with the composition calculated from the temperature readings closest to the opening of the center tap. ●, average increase in alcohol content calculated from the measurements during the experiments. For conversion of the temperature data into an alcohol content we used the liquidus relation displayed in Figs A1 and A2.

20 min (as calculated from the growth law), the alcohol content has increased significantly (0·4 ± 0·2 wt %). Using the liquidus of Fig. A2b (see the Appendix) the associated depressed liquidus temperature is found to be –7·15 ± 0·15°C. Within error, this is identical to the observation of the depressed interface temperature reported above (–7·22 ± 0·13°C) and we therefore do not measure any significant undercooling, which would also be associated with an extensive thermal boundary layer. However, considering the uncertainties in the compositional measurements we cannot rule out the existence of a small thermal boundary layer with an accompanying small temperature gradient. Furthermore, to drive crystal growth there has to be undercooling, but its amplitude is clearly smaller than the resolution of our measurements.

To investigate further the possibility of true undercooling, the temperature measurements described above can be compared with the composition measurements at the center tap (see Fig. 7b). For this, the temperature measurements at thermocouple 7 (the thermocouple that is closest to the center tap; see Fig. 2) of all runs whose mush thickness is displayed in Fig. 6 are converted into an equivalent alcohol content (fine lines in Fig. 7b) using the phase diagram. This assumes the melt is everywhere in local thermodynamic equilibrium. To compensate for the effect of the slightly different locations of thermocouple 7 and for the tap opening, the time axis is nondimensionalized. That the converted temperatures match the observed mean increase in alcohol content as well as they do is consistent with equilibrium crystallization. Crystallization exhibiting a large disequilibrium and undercooling on the other hand would not show this similarity. This observation clearly favors the first of the three possibilities: the observed thin alcohol-enriched layer is a result of our inability to detect the true mush–melt interface and of a compositionally and thermally stratified boundary layer. The latter is easily verified by calculating the density profile across this layer. Part of this thin enriched layer, as indicated by a simple model calculation, is due to diffusion and mechanical expulsion of alcohol from the expanding ice, and the rest is due to a small degree (1–2%) of visually undetectable crystallization. Importantly, the liquid appears to be in thermodynamic equilibrium everywhere in this layer. Moreover, we do not detect any enrichment of alcohol in the bulk liquid, which rules out efficient mixing of this layer with the rest by sustained turbulent convection and erosion.

Measurement of the convective motion

In nine separate experiments long-exposure photographs were taken after 25 min, 4 h, and 9·5 h to determine a mean convective velocity in the fluid. Three examples are shown in Fig. 8. Here it is of interest to note that the flow patterns observed after 25 min and 4 h are highly variable, whereas the flow patterns observed in the three experiments after 9·5 h look more or less the same, i.e. convective motion in the interior driven by narrow upwellings along the sides of the tank. The streak length in each photograph (Fig. 8) reflects both convective velocity and exposure time (i.e. 5 s, 15 s, 25 s, respectively); the calculated mean velocities are given in Table 1. The initial mean velocity is ~1·0 mm/s (after 25 min), dropping to ~0·25 mm/s after 4 h, and to ~0·05 mm/s after 9·5 h; overall, the velocity decreases by a factor of 20 during the first 10 h of the experiment. Most of the motion in the last image (Fig. 8c) appears to be confined to the sidewalls of the tank, and is related to the slight, but as already noted, important unwanted heat flux into the system through the tank walls.

In addition to the determination of the mean velocities we also measured the velocity distribution in the flow

Table 1: Mean and r.m.s. values of convective velocities in nine experiments

Experiment	Mean velocity (mm/s) after		
	25 min	4 h	9·5 h
RUN63	1·09 ± 0·45	—	—
RUN64	—	0·20 ± 0·06	—
RUN65	—	—	0·06 ± 0·03
RUN66	1·00 ± 0·67	—	—
RUN67	—	0·26 ± 0·10	—
RUN68	—	—	0·06 ± 0·03
RUN69	1·00 ± 0·40	—	—
RUN70	—	0·27 ± 0·12	—
RUN71	—	—	0·05 ± 0·02

along the sidewalls at 9·5 h (see Fig. 9). The data show some scatter, especially near the maximum velocity, but nevertheless there is clearly a more or less steady increase in velocity with distance from the wall, reaching a maximum of 0·017 cm/s at ~1 cm. Beyond this point the velocity decays at a faster than linear rate with increasing distance from the wall. The peak velocity is about 2–3 times larger than the mean velocity determined earlier (see Table 1). From these values and the values of material variables relevant to the experiment (see Table 2) one can readily calculate local Reynolds and Peclet numbers for this wall flow. The Reynolds number is ~6 (based on the large-scale flow, assuming a shear flow with a length scale of 3 cm, it is about unity) which is, however, no proof for a non-turbulent flow, as shown by Tilgner *et al.* (1993), who found the Reynolds number for a shear flow during a convection experiment at $Ra = 1{\cdot}1 \times 10^9$ to be about 50. The large-scale Peclet number is about 360, which indicates the dominance of advective heat transport.

COMPARISON OF THE DATA WITH A THEORETICAL MODEL

A general one-dimensional (1D) model for the solidification of a fluid cooled from above has been developed by Huppert & Worster (1992). Here we briefly describe their model and then modify it to allow for heat flow into the system through the walls. We will show that the sidewall inflow of heat significantly affects the mush layer thickness (see Fig. 6), bulk liquid temperature, and Rayleigh number. The model description and extensions are followed by a discussion of the application of this model to data gathered in the experiments themselves.

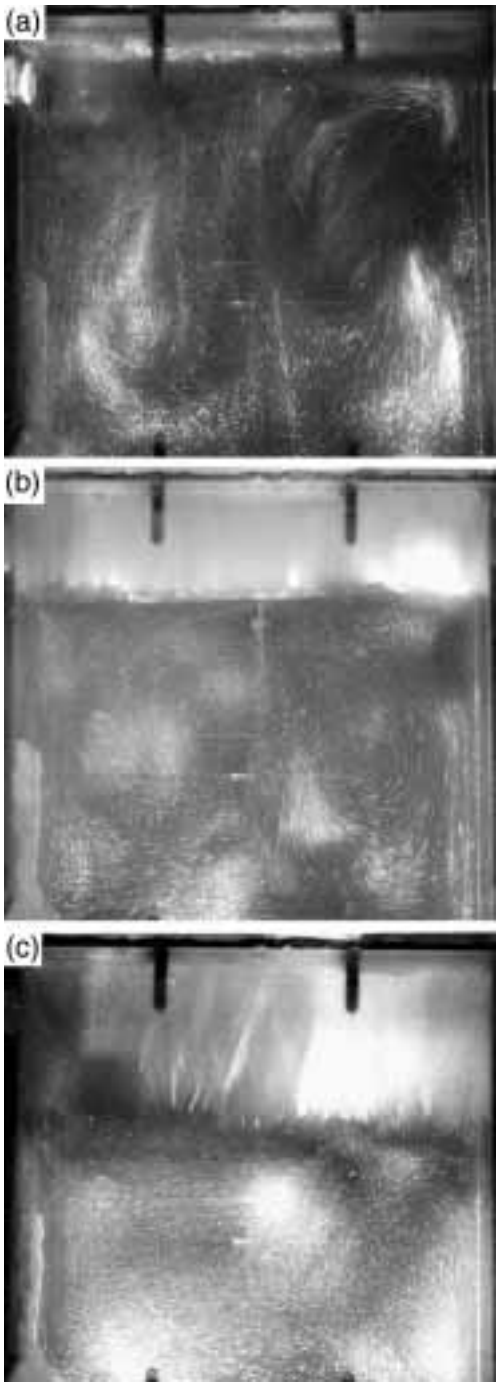

Fig. 8. Three time-lapse images of the convective motion in the tank taken after 25 min (a), 4 h (b), and 9·5 h (c). The blurriness is due to mist that forms on the Plexiglas tank immediately upon exposure to room air. The exposure times are 5 s (a), 15 s (b), and 25 s (c), respectively.

Table 2: Values of variables used to calculate the evolution of the experiment

Variable	Description	Value	Units	Source
c_s	specific heat solid	1832	kJ/m^3 per °C	Weast (1970), Kaye & Laby (1986)
c_l	specific heat liquid	3912	kJ/m^3 per °C	Washburn (1929)
k_s	thermal conductivity of solid	2·2	W/m per °C	Kaye & Laby (1986), Ross *et al.* (1978)
k_i	thermal conductivity of liquid	0·37	W/m per °C	Vargaftik (1983)
k_f	thermal conductivity of insulation	0·039	W/m per °C	Manufacturer
k_p	thermal conductivity of Plexiglas	0·21	W/m per °C	Manufacturer
L	latent heat	306000	kJ/m^3	Lide (1992)
ν	kinematic viscosity	$5{\cdot}7 \times 10^{-6}$	m^2/s	Kerr *et al.* (1990*a*)
κ_l	thermal diffusivity of liquid	$9{\cdot}48 \times 10^{-8}$	m^2/s	calculated
G	growth constant	$2{\cdot}2 \times 10^{-6}$	m/s per °C	Kerr *et al.* (1990*a*)
T_b	top plate temperature	−20	°C	
T_{fr}	fridge temperature	0 or −4·5	°C	
T_L (C_0)	liquidus temperature	−6·95	°C	
C_0	initial composition	83·2	wt %	
C_s	solid composition	100·0	wt %	
C_b	composition at T_b	58·0	wt %	
Δx_f	thickness of insulation	3·8	cm	
Δx_p	thickness of Plexiglas	1·85	cm	
H	height of tank	20·2	cm	

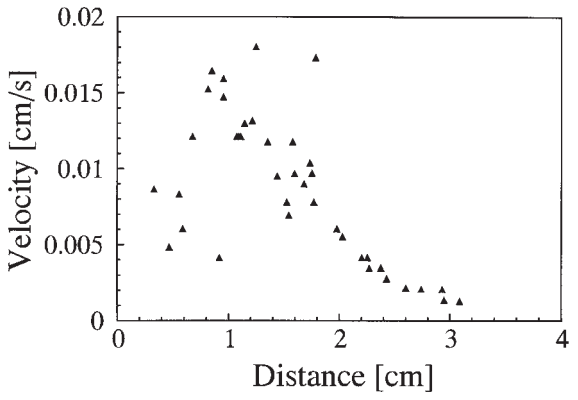

Fig. 9. Velocity distribution in the mechanical boundary layer along the sidewalls of the tank at 9·5 h. The velocities were determined by measuring streak length from Fig. 8c and two other photographs along a horizontal profile perpendicular to the sidewalls of the tank.

Model formulation

A schematic diagram of the model setup is shown in Fig. 10. There are two basic models: an equilibrium model and a kinetic model; each is discussed below. In both models the mush extends down from the cooled top of the system to a depth $h(t)$. Conservation of heat in the mush requires

$$c_m \frac{\partial}{\partial t} T = \frac{\partial}{\partial z}\left(k_m \frac{\partial}{\partial z} T\right) + L \frac{\partial}{\partial t}\phi \tag{1}$$

with

$$c_m = \phi c_s + (1-\phi) c_l \tag{2}$$

$$k_m = \phi k_s + (1-\phi) k_l. \tag{3}$$

This assumes that the mush can be treated as a continuum, whose thermal properties are only a function of the fraction crystallized, ϕ. In these equations c and k are the specific heat per unit volume and thermal conductivity, with the subscripts l, m and s indicating liquid, mush, and solid properties, respectively. L is the latent heat of fusion per unit volume, T is temperature, t is time, and z is the vertical downward coordinate.

Conservation of mass of solute in the mush is given by (e.g. Kerr *et al.*, 1990*a*)

$$(1-\phi)\frac{\partial}{\partial t} C = (C - C_s)\frac{\partial}{\partial t}\phi \tag{4}$$

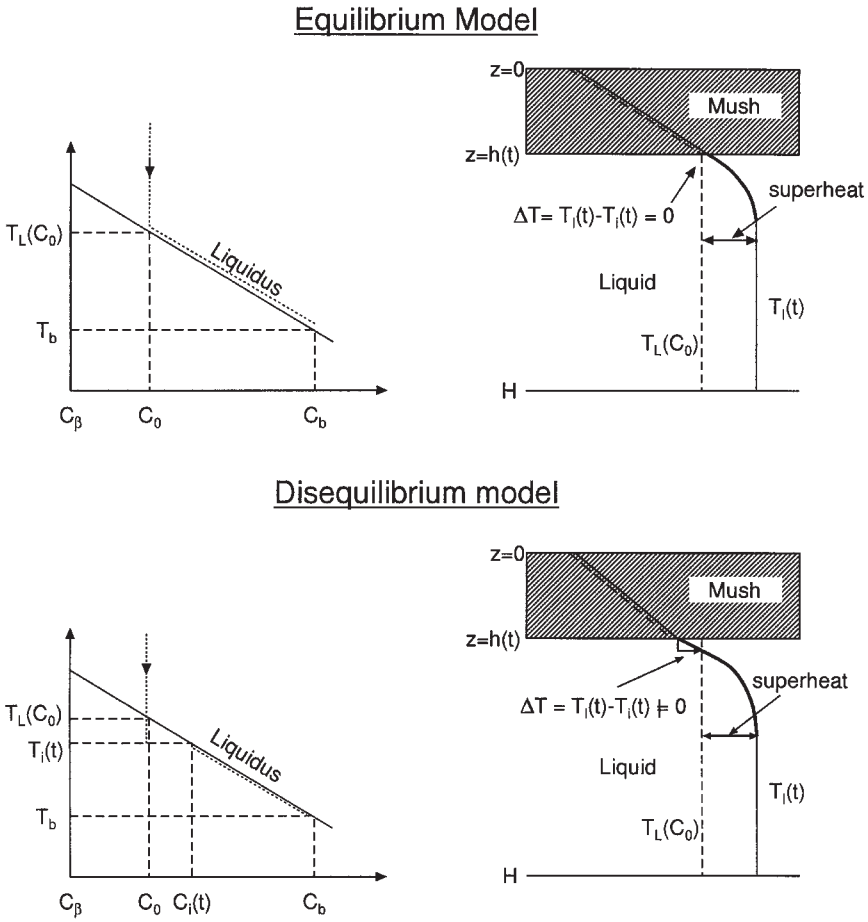

Fig. 10. Schematic diagram of the theoretical models. Variables used in the analysis are depicted here. The critical difference between these two models is in the degree of undercooling assumed associated with growth of the mush layer. The accompanying phase diagrams on the left show the relation of temperature to composition.

where C is the amount of water in wt % in the liquid and C_s is the composition of the solid precipitating from the melt which is pure ice (i.e. $C_s = 1$). Solute transport in (4) in the vertical direction by diffusion or other means is neglected, which is a valid approximation to our system. Equations (1) and (4) are coupled through the linear liquidus relationship:

$$T_l(C) = aC + d \tag{5}$$

where a and d are constants determined by the phase diagram. In the present case $a \sim -0{\cdot}52$°C/wt % and $d \sim 1{\cdot}75$°C. (We also implemented and tested a quadratic dependence of the liquidus on the composition, but as the results are almost identical, here we employ the more simple linear formulation.)

Conservation of heat at the mush–melt interface requires (e.g. Kerr *et al.*, 1990*a*)

$$(c_l(T_l - T_i) + L\phi_i)\frac{\mathrm{d}}{\mathrm{d}t}h = k_m\frac{\partial}{\partial z}T\bigg|_{z=h^-} - F_T \tag{6}$$

where T_l and T_i are, respectively, the temperatures of the underlying liquid and at the mush interface; ϕ_i is the fraction crystallized at the interface, and F_T is the convective heat flux transferred from the fluid into the mush.

The magnitude of F_T can be estimated from the well-known Nusselt–Rayleigh number relationship Nu $\propto$ $\mathrm{Ra}^{1/3}$ (e.g. Kraichnan, 1962; Turner, 1979; Turcotte & Schubert, 1982), in which case the heat flux is given by

$$F_T = 2^{4/3}\lambda k_l\left(\frac{\alpha_0 g}{\kappa_l \nu}\right)^{1/3}\left(\frac{\alpha_T}{\alpha_0}\right)^{1/3}(T_l - T_i)^{4/3} \tag{7}$$

This formulation of the heat flux is the same as that used

by Kerr *et al.* (1990*a*, 1990*b*), but we explicitly include the temperature dependence of α (the coefficient of thermal expansion). The dependence of α on T has been carefully measured by Kerr *et al.* (1990*a*) [$\alpha_T = 10^{-4}(2{\cdot}25 - 0{\cdot}15T)$]. g is the acceleration due to gravity, α_0 is the coefficient of thermal expansion at the initial temperature T_0, κ_l is the thermal diffusivity of the liquid, and ν is the kinematic viscosity of the liquid. Kerr *et al.* (1990*a*) took λ to be constant and equal to 0·056, which is the asymptotic limit for high-Ra convection, when in fact it has been found to increase with decreasing Ra (e.g. Long, 1976; Denton & Wood, 1979). Here we implement the formulation suggested by Long (1976) for water and with the fitting constant $s = 1/3$

$$\mathrm{Nu} = \lambda \mathrm{Ra}^{1/3} \text{ with } \lambda = \frac{0{\cdot}04356}{[1 - 1{\cdot}402 \times (\mathrm{Ra} \times \mathrm{Nu})^{-1/12}]^{4/3}}. \tag{8}$$

This makes the heat transfer across the interface at small Ra more efficient. This formulation seems more appropriate in light of the possibility of smaller governing Rayleigh numbers.

Finally, the temperature of the bulk liquid below the growing mush is calculated from

$$c_l(H-h)\frac{\mathrm{d}}{\mathrm{d}t}T_l = -F_T \tag{9}$$

where H is the initial thickness of the fluid layer.

So far still missing in this formulation is the additional heat leaking through the tank walls as a result of insufficient insulation, which must be accounted for in equations (1) and (9). The amount of heat leaking into the system is proportional to the thermal resistance f of the compound wall consisting of Plexiglas and closed cell foam insulation:

$$f = \left(\frac{\Delta x_f}{k_f} + \frac{\Delta x_p}{k_p}\right). \tag{10}$$

Here k_p and k_f are the thermal conductivities of, respectively, the Plexiglas and foam, and Δx_p and Δx_f are the respective wall thicknesses. In general one also wants to take into account the thermal resistance caused by natural convection of the air in the refrigerator, but because of forced circulation of this air by a fan (see section on Experimental setup), we can neglect this effect. The extended model equations (1) and (9) now take the following forms:

$$c_m\frac{\partial}{\partial t}T = \frac{\partial}{\partial z}\left(k_m\frac{\partial}{\partial z}T\right) + L\frac{\partial}{\partial t}\phi + Q \tag{11}$$

and

$$c_l(H-h)\frac{\mathrm{d}}{\mathrm{d}t}T_l = -F_T + F_p. \tag{12}$$

Here Q is a heat source term that is used in this 1D model to account for any lateral heat flux through the compound walls of the system into the mush. It is obtained by appropriate averaging of the heat diffusion terms in the full energy equation over the horizontal area of the mushy layer. Assuming a steady heat flux through the compound walls of the tank, we can evaluate this heat source as

$$Q = -\frac{4}{fX}(T - T_j) \tag{13}$$

where X is the width of the tank and T_f is the temperature maintained on the outside of the insulation (here either 0°C or –4·5°C). The factor four occurring in (13) is due to the four sidewalls of the tank, which are in contact with the mush.

F_p in (12) is the heat flux through the tank walls and bottom into the system, and is simply

$$F_p = \frac{(T_f - T_l)}{f}\left(1 + 4\frac{H-h}{X}\right). \tag{14}$$

The numerical factor one occurring inside the parentheses of (14) is the heat flux through the bottom of the tank, and the numerical constant four again accounts for flow through the four sidewalls. In a perfectly insulated system ($f = \infty$), Q and F_p vanish. As will be shown below, the inclusion of this additional heat flow into these model calculations is completely consistent with our measurements.

Like Kerr *et al.* (1990*a*, 1990*b*) we render the governing equations dimensionless by scaling the length with H, time with H^2/κ_l and the temperatures with $\Delta T = T_L(C_0) - T_b$ and then $\theta = [T - T_L(C_0)]/\Delta T$. Here C_0 is the initial composition of the melt, and T_b is the temperature at the cooled top. Furthermore, we make use of the fact that our tank is cubic, i.e. $H = X$. Combining (4), (5) and (11) we find

$$c\frac{\partial}{\partial t}\theta = \frac{\partial}{\partial z}\left(k\frac{\partial}{\partial z}\theta\right) - f'(\theta - \theta_{fr}) \quad (0 \le z \le h) \tag{15}$$

with

$$k \equiv \phi \frac{k_s}{k_l} + 1 - \phi \tag{16}$$

$$c \equiv \phi \frac{c_s}{c_l} + 1 - \phi + \frac{S}{\mathscr{C}}(1-\phi)^2 \tag{17}$$

$$f' = \frac{4H}{fk_l} \tag{18}$$

and

$$\phi = \frac{-\theta}{\mathscr{C} - \theta} \tag{19}$$

with

$$S = \frac{L}{c_l \Delta T}, \quad \mathscr{C} = \frac{C_s - C_0}{C_0 - C_b}. \tag{20}$$

The interface location is found by solving

$$(S\phi_i + \theta_l - \theta_i)\frac{\mathrm{d}}{\mathrm{d}t}h = k\frac{\partial}{\partial z}\theta\bigg|_{z=h^-} - \mathrm{Nu}^*\lambda(\theta_l - \theta_i)^{4/3}(a' + b\theta_l)^{1/3} \tag{21}$$

and the temperature in the bulk liquid underlying the mush follows from

$$\frac{\mathrm{d}}{\mathrm{d}t}\theta_l = -\frac{1}{1-h}[\mathrm{Nu}^*\lambda(\theta_l - \theta_i)^{4/3}(a + b\theta_l)^{1/3}] - \frac{f'}{4}\frac{[1 + 4(1-h)]}{1-h}(\theta_l - \theta_{fr}). \tag{22}$$

Here $\mathrm{Nu}^* = (\mathrm{Ra}_0/\theta_0)^{1/3}$, $\mathrm{Ra}_0 = \alpha_0 g[T_0 - T_L(C_0)]H^3/\kappa_l \nu$, and a' and b are coefficients given by $a' = \alpha[T_L(\mathscr{C})]/\alpha_0$, and $b = (\mathrm{d}\alpha/\mathrm{d}T) \times \Delta T/\alpha_0$.

These equations are subject to the following boundary and initial conditions [including (21)]:
(a) equilibrium growth

$$\begin{gathered} \theta = -1 \quad (z=0) \\ h = 0, \quad \theta_l = \theta_0 \quad (t=0) \\ \theta_i = 0, \quad \phi_i = 0, \quad C_i = C_l \quad [z = h(t)] \end{gathered} \tag{23}$$

(b) interfacial or kinetic growth law (Kerr *et al.*, 1990*b*)

$$\begin{gathered} \theta = -1 \quad (z=0) \\ h = 0, \quad \theta_l = \theta_0 \quad (t=0) \\ \theta = \theta_i, \quad \phi_i = \phi(\theta_i) \quad [z = h(t)]. \end{gathered} \tag{24}$$

Here ϕ_i is the fraction solid at the interface. In the latter case, in addition to the interfacial boundary conditions at $z = h(t)$, an interfacial growth law is needed, which may be derived by taking a closer look at the mush–melt interface. As this interface consists of many tiny crystals, its rate of advance may be expressed by the growth rate of the crystals forming the interface. This neglects the fact that two processes, nucleation and crystal growth, are responsible for the advance of the interface, which is a commonly made assumption (e.g. Worster *et al.*, 1993).

The crystal growth rate U is typically described as a thermally activated processes

$$U \propto \exp\left(-\frac{\Delta G_t}{RT}\right)\left[1 - \exp\left(-\frac{\Delta G_v}{RT}\right)\right] \tag{25}$$

where ΔG_t is the activation energy for diffusion and ΔG_v is the difference in the Gibbs free energy between the liquid and the solid state, which is known as the driving force behind nucleation and crystal growth. For small deviations from the thermodynamic equilibrium temperature, the Gibbs energy liberated per transformed unit volume, ΔG_v, is related to the degree of undercooling below the thermodynamic equilibrium temperature T_e (e.g. Kirkpatrick, 1981) through $\Delta G_v = \Delta H_v \times \Delta T_u/T_e$ (this holds only for small undercoolings, ΔT_u); here ΔH_v is the enthalpy difference between the solid and the liquid state and ΔT_u is the undercooling below the thermodynamic equilibrium temperature T_e. Dropping all but the constant for the Taylor series expansion of the first term in (25) and keeping the constant and linear term for the expansion of the second term leads to a linear relationship between crystal growth U rate and undercooling ΔT_u

$$U \propto \frac{\Delta G_v}{RT} = \frac{\Delta H_v \Delta T_u}{RT\,T_e} \tag{26}$$

indicating that it is ΔG_v that drives nucleation and crystal growth and not the undercooling (ΔT_u). Assuming now that the crystal growth rate is representative of the rate $\mathrm{d}h/\mathrm{d}t$ at which the interface advances, we may write as first approximation for the growth rate of the mush

$$U \propto \frac{\mathrm{d}}{\mathrm{d}t}h = \mathscr{G}(T_L - T_i) \tag{27}$$

where $\mathscr{G}$ is a constant (its temperature dependence has been neglected), which Kerr *et al.* (1990*b*) have shown experimentally to be equal to $2{\cdot}2 \times 10^{-6}$ m/s per °C for the water–isopropanol mixture. Rendering this equation dimensionless gives

$$\frac{\mathrm{d}}{\mathrm{d}t}h = -\gamma\theta_\mathrm{i} \tag{28}$$

where

$$\gamma = \frac{\Delta T H}{\kappa_\mathrm{l}}\mathscr{G}. \tag{29}$$

The nonlinear heat conduction equation (15) is solved by mapping the interval [0,$h(t)$] linearly onto [0,1], and then using an iterative Crank–Nicolson technique. Accuracy is provided using 50 grid points in the finite difference solutions of the equilibrium model. In the case of the interfacial growth law we used 40 grid points, which provides sufficient accuracy. In the case of equilibrium growth a fourth-order Runge Kutta method is implemented for the integration of the two remaining ordinary differential equations (ODEs), (21) and (22). Here, following Kerr *et al.* (1990*a*), we rewrite the equations in terms of h^2 to overcome the singularity at $t = 0$. Solving the set of equations with the interfacial growth law we substitute (28) into (21) and solve it together with the heat conduction equation (15) for varying θ_i until (21) is satisfied to a prescribed accuracy. Here the root of (21) is sought using a combined root bracketing, bisection, and inverse quadratic interpolation method, also known as Brent's method (e.g. Press *et al.*, 1992). For the remaining ODEs, (22) and (28), we again use a fourth-order Runge Kutta method. Both algorithms (the equilibrium model and the kinetic growth model) were tested for convergence and stability. The code was validated in two ways: first, through solving the equations by a second, numerically different method; second, M. G. Worster (personal communication, 1993) kindly provided some numerical data on the equilibrium model, which we matched against our own code.

In addition to the general validation of the code itself, the significance and proper implementation of the heat flux through the tank walls was validated in two ways: first, by computing the evolution of the bulk liquid temperature in the tank assuming a top plate temperature of –6°C (i.e. no solidification) and an external tank temperature of $T_\mathrm{f} = 0$°C. After 15 h the model predicts a bulk liquid temperature of –5·6°C, which is almost exactly the temperature (–5·55°C) measured in the experiment specifically designed to evaluate this influence (see the Experimental setup section). This also confirms that neglecting the thermal resistance caused by thermal convection in the air of the refrigerator [see equation (10)] is an appropriate assumption.

Second, we subtract the experimental results of a 0°C wall experiment from the results of a –4·5°C wall experiment. This gives the differences in crust thickness and bulk liquid temperature solely caused by the different amount of heat flowing through the sidewalls. Next, exactly the same subtraction procedure is followed in the calculations using the equilibrium model: once with the 0°C wall and once with the –4·5°C wall. Figure 11 shows a comparison of the observed and theoretical differences, which are found to be in close agreement once the superheat has been removed from the fluid. The simplified 1D model obviously does not capture the complexity of the thermal history during the first 8 h; this is characterized by turbulent thermal convection and a quickly changing bulk liquid temperature, which makes the steady-state heat flux across the sidewalls a crude assumption for this period during the experiment (Fig. 11b). For the differences in mush thickness we only show the differences for $t > 10$ h, as our linear models for the mush thickness are representative only for $t > 7$ h.

Model calculations

Most of the general features of this type of model have been described in some detail by Kerr *et al.* (1990*a*, 1990*b*) and Huppert & Worster (1992). Here we focus on the effects of extraneous heat flow into the system and the importance of convective heat transport during solidification. We begin by showing the results of calculations for the equilibrium model neglecting and including convective and side-wall heat flow, which is central to understanding the experiments. Next we turn to the results of model calculations based on the interfacial growth law. Last, we consider the Rayleigh numbers determined from the model calculations and the measurements of convective velocity. We find that most, if not all, of the post superheat convective motion observed in the experiments is attributable to the sidewall inflow of unwanted heat. Unless otherwise stated, Table 2 lists all the values of variables used in the model calculations.

Equilibrium model

To demonstrate both the importance of the convective heat flow from the bulk liquid into the mush during the early stages of the experiments and the relevance of the heat flow through the walls of the system, the results of four types of equilibrium model calculations are compared in Fig. 12. The main deficiency of the purely conductive model with no convective flux from the bulk liquid into the mush region (continuous line in Fig. 12a) and no sidewall inflow of heat is that the bulk liquid temperature remains constant at 0°C (not shown) and the calculated mush thickness is significantly thicker early on and slightly thinner at late times.

The equilibrium model including the convective heat flux across the mush–liquid interface (dashed lines in Fig. 12) overestimates the mush thickness at late times, but matches the observed temperature in the bulk liquid

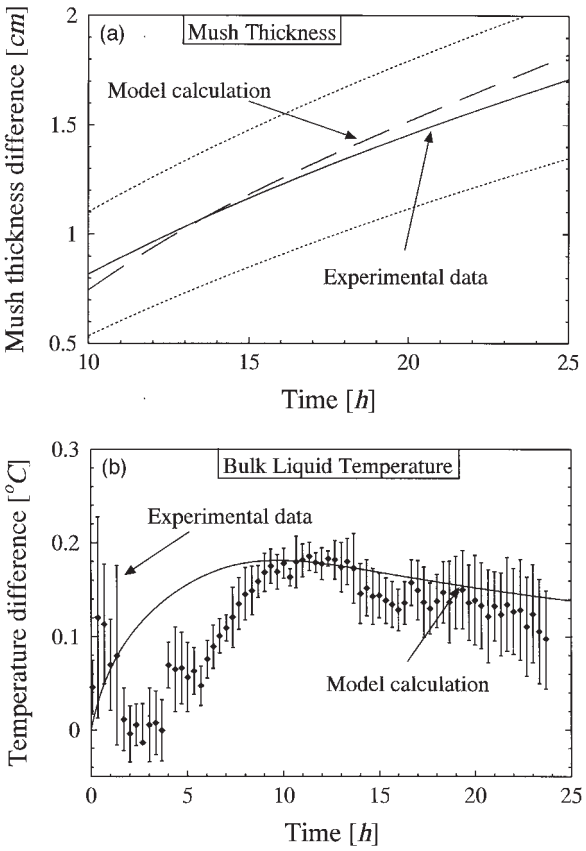

Fig. 11. Difference in mush thickness (a) as well as bulk liquid temperature (b) for the experiments carried out with a 0°C boundary condition and the –4·5°C boundary conditions. The continuous line in (a) is a subtraction of the growth law determined for the 0°C wall experiments from the growth law for the –4·5°C experiments (see also Fig. 6), the dotted lines give the uncertainty. The dashed line in (a) is the difference between two equilibrium model calculations, one carried out with a 0°C wall, the other with the –4·5°C wall. In (b) we give the difference in bulk liquid temperature. We calculated all possible differences between the 0°C and –4·5°C rims (in all 40 differences per point shown) and determined a mean temperature difference with its standard deviation, which is based on only the scatter of the data and not on the uncertainty in thermocouple calibration (see section on Experimental setup). We compare these values with the difference determined from the model calculations (continuous line).

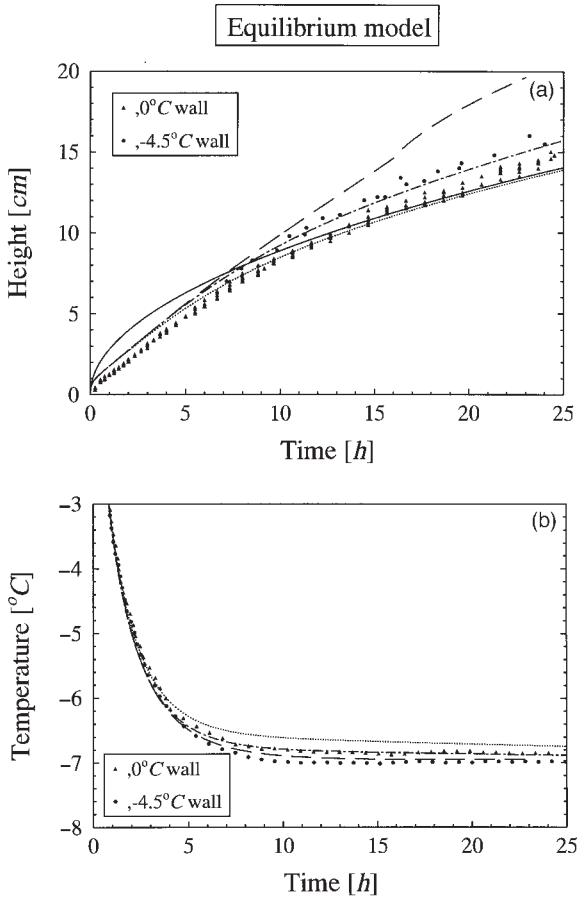

Fig. 12. Crust thickness (a) and bulk liquid temperature (b) for four types of model calculations using the equilibrium model. The continuous line represents results assuming no convection (i.e. pure conduction), the dashed line represents results assuming a convective heat flux from the bulk liquid into the mush but no sidewall heat flow. Adding sidewall heat flow to the calculation, the results assuming a –4·5°C wall are shown by the dash–dotted line, whereas the dotted lines show the results assuming a 0°C wall. The triangles are the data from the 0°C experiment, the circles are from the –4·5°C experiment.

underlying the mush. The reason for this fast mush growth stems from an analytical logarithmic singularity of the mushy layer thickness as the superheat tends towards zero (e.g. Worster, 1991). The kink in the dashed line after about 16 h is due to ceasing convection, as the Rayleigh number drops below its critical value.

The effect of sidewall inflow of heat is addressed in the next two calculations, shown in Fig. 12 as dash–dotted and dotted lines. The dash–dotted line shows the results of calculation made assuming a wall temperature of –4·5°C, and the accompanying dotted line shows the results assuming a 0°C wall. Comparing the model with no sidewall heat flow (dashed lines) with these two calculations with different wall temperatures (dotted and dash–dotted lines) clearly demonstrates that a rising wall temperature raises the bulk liquid temperature and reduces mush thickness. The additional inflow of heat through the walls prevents the temperature in the bulk liquid from dropping as quickly as in the former model and, with more remaining superheat, mush growth is slower.

One general feature of all equilibrium models including the effect of sidewall heat flow is that they overestimate the temperature in the bulk liquid stirring after about 4–5 h. Furthermore, in contradiction to the measurements, the calculated bulk liquid temperature continually decreases, albeit slowly, with time, whereas the

experiments themselves do indicate a nearly constant bulk liquid temperature after about 10 h.

Disequilibrium model

In Fig. 13 we contrast four disequilibrium model calculations based on the interfacial growth law; the effects of variations in interfacial growth law constant $\mathscr{G}$ and sidewall inflow of heat are delineated. The model without the additional sidewall heat flow and $\mathscr{G} = 2{\cdot}2 \times 10^{-6}$ m/s per °C [as determined and used by Kerr *et al.* (1990*b*)] underestimates the bulk liquid temperature by ~0·7°C (bold dashed line in Fig. 13b) relative to that observed in the set of experiments carried out with the –4·5°C boundary temperature (circles in Fig. 13b). The constant temperature after about 9 h is due to the fact that the interface temperature (fine dashed line in Fig. 13), which is not fixed in this model [see equations (21) and (28)], becomes larger than the temperature of the underlying bulk liquid, and the system is henceforth stably stratified, i.e. convection ceases. This feature of ceasing convection has also been noted by Kerr *et al.* (1990*b*) in their model calculations, although they did not quantify it. It should be noted here that our measurement of the convective velocities clearly shows convection in the experiment after 9 h, which we attribute almost exclusively to the sidewall heat flow (see below). This model also fails to explain the mush thickness, which should be compared with the data gathered with the –4·5°C boundary temperature (see circles in Fig. 13a).

Adding the sidewall heat flux to this model [dash–dotted (–4·5°C wall) and dotted (0°C wall) lines in Fig. 13] reduces the mush thickness below the observed values (i.e. the triangles in Fig. 13a). In general, the effect of raising the wall temperature is the same as discussed above for the equilibrium model, i.e. it increases bulk liquid temperature and decreases mush thickness. We find that in the cases of sidewall inflow of heat the temperature of the bulk liquid goes through a local minimum at about 7 h before it reaches approximately –7·05°C after about 25 h (for the 0°C wall, see bold dotted line in Fig. 13b). This kind of behavior (i.e. going through a local minimum) is not observed in the experiments themselves. Its occurrence in the model calculation can be explained by the interplay of sidewall heat flow, convection, and the temperature difference between the bulk liquid and the mush–liquid interface. During initial cooling this temperature difference is large and convection is very efficient. As the mush growth rate is small (the constant $\mathscr{G}$ in the growth law is small), the interface temperature remains low and the bulk liquid can supercool. As the mush becomes thicker, the growth rate slows, which is assured by raising the interface temperature [see (28)], resulting in a decreasing temperature difference between the bulk liquid and the interface. This makes convection increasingly inefficient, and the sidewall heat flow starts to increase the bulk liquid temperature slightly. Eventually a state of near-equilibrium is maintained that satisfies all the factors involved (bulk liquid temperature, interface temperature, convection and sidewall heat flow). In both cases (–4·5 and 0°C wall) the mush–heat interface temperature (see bold dash–dotted and fine dotted lines in Fig. 13b) remains below the bulk liquid temperature and therefore convection is always present.

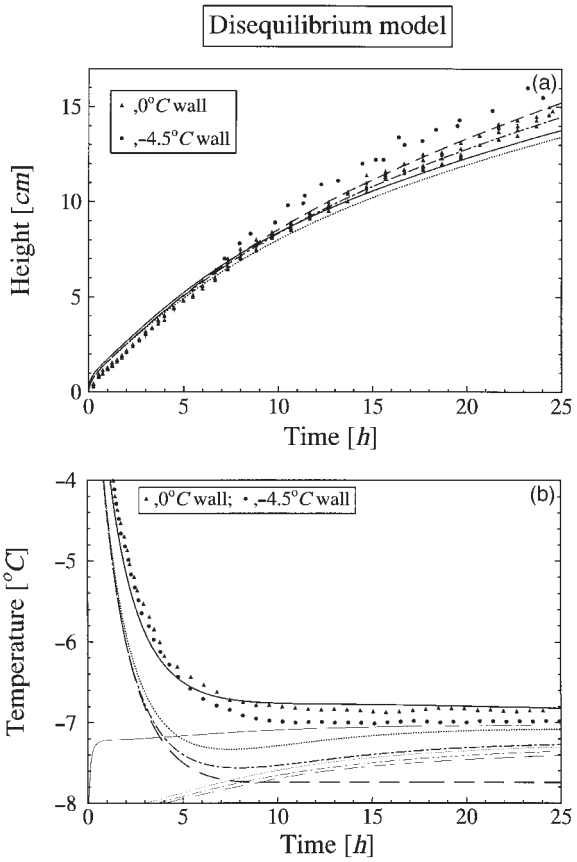

Fig. 13. Crust thickness (a) and bulk liquid temperature (bold lines) and interface temperatures (fine lines coming from base) (b) for four disequilibrium model calculations based on the interfacial growth law. The dashed lines represent a calculation using $\mathscr{G} = 2{\cdot}2 \times 10^{-6}$ m/s and no heat flow through the walls of the system. The model calculation including the heat flow through the sidewalls (–4·5°C wall) is given by the dash–dotted line ($\mathscr{G} = 2{\cdot}2 \times 10^{-6}$ m/s per °C). The dotted line represents the results of a calculation assuming $\mathscr{G} = 2{\cdot}2 \times 10^{-6}$ m/s per °C and a wall temperature of 0°C. The continuous line gives the result of a calculation including sidewall heat flow (0°C wall) for an increased value of $\mathscr{G} = 10^{-5}$ m/s per °C.

Increasing $\mathscr{G}$ from $2{\cdot}2 \times 10^{-6}$ to 10^{-5} m/s per °C (continuous lines in Fig. 13) gives good agreement between the measured and calculated bulk liquid temperature (see bold continuous line in Fig. 13b). The temperature of the mush–melt interface (fine lines in Fig. 13b), is almost

constant after 10 h and varies only between –7·1 and –7·0°C. The increase in temperature as discussed for a value of $\gamma = 2{\cdot}2 \times 10^{-6}$ m/s per °C is gone, and it can be shown that a value of $\gamma \sim 8 \times 10^{-6}$ m/s per °C results in a slight temperature increase around 18–20 h as is seen experimentally (see dashed line in Fig. 3). Although this model obviously does very well in explaining the observed temperatures, it still underpredicts the mush thickness somewhat. There does not appear to be a single value of γ that fits both the temperature and the mush thickness measurements. The temperature data suggest a value of γ between 5×10^{-6} and 10^{-5} m/s per °C, whereas, to obtain the correct mush thickness, γ can never be large enough. Increasing γ is equivalent to approaching an equilibrium situation.

Comparison

Of all of the equilibrium and kinetic model calculations presented in Figs 12 and 13, the equilibrium calculation and the kinetic model with the high growth law constant come closest to the measured values. For comparison, Fig. 14 shows the best fit equilibrium and disequilibrium ($\gamma = 10^{-5}$ m/s per °C) models. In terms of crust thickness both models are almost exactly the same, whereas in terms of the bulk liquid temperature the kinetic model gives a slightly better fit.

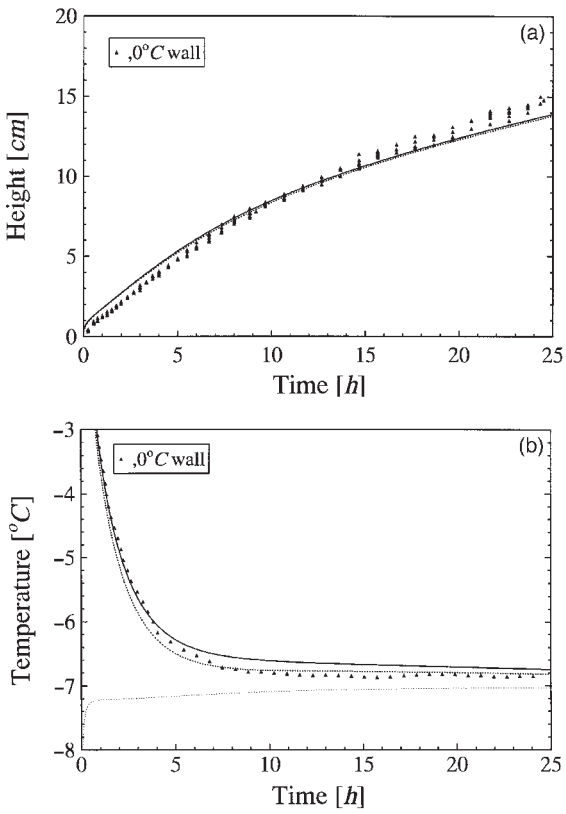

Fig. 14. Best fit equilibrium (continuous lines) and disequilibrium (dotted lines) model calculations for the 0°C wall experiments. The triangles show the measured crust thickness (a) as well as the bulk liquid temperature (b). In the disequilibrium model, we used a value of 10^{-5} m/s per °C for γ. The bold lines in (b) give the bulk liquid temperature, the fine line the interface temperature in the disequilibrium model. In the case of the equilibrium model the interface temperature is always equal to the liquidus temperature (not shown).

Calculated Rayleigh numbers

As a result of the parameterization of convective heat transfer in the 1D model used above, we do not have direct access to convective velocities inside the bulk liquid from the modeling side but we can calculate the thermal Rayleigh number driving the convective flow from the model calculations (see Fig. 15), to describe the flow in terms of turbulence. The continuous line in Fig. 15 represents the decrease in Ra calculated for both the equilibrium and disequilibrium models (using the best estimate of $\gamma = 10^{-5}$ m/s per °C) including sidewall heat flow (0°C wall); these coincide at this scale, and therefore only a single curve is shown. Initially, the thermal Rayleigh number is well into the hard turbulence regime, which begins at $Ra > 4 \times 10^7$ (e.g. Heslot *et al.*, 1987). After about 1·5 h the model calculations indicate a thermal Rayleigh number of less than 4×10^7, putting the convective motion into the so-called soft turbulence regime $2 \times 10^5 < Ra < 4 \times 10^7$ (e.g. Heslot *et al.*, 1987), where it stays till the end of the experiment. The second model calculation (dashed line in Fig. 15) is an estimate for the thermal Rayleigh number associated with convection driven purely by the sidewall and bottom inflow of heat. This model calculation suggests that for $t > 10$ h this calculated Rayleigh number is consistent with a residual flow caused by heating from the sides and below.

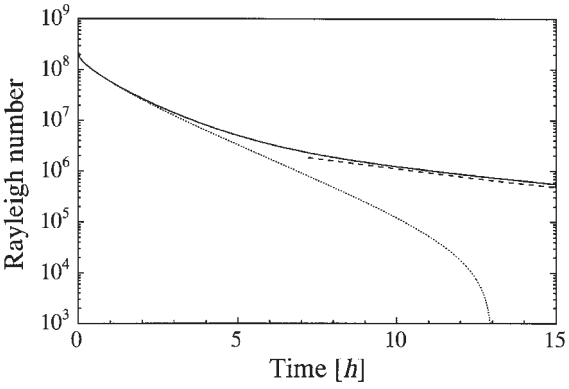

Fig. 15. Calculated Rayleigh numbers as a function of time. The continuous line shows the temporal evolution of the Rayleigh number in model calculations including the sidewall inflow of heat. The dotted line, in contrast, gives the temporal evolution of the Rayleigh number for a perfectly insulated system. The dashed line represents the Rayleigh number associated with the convection in a fluid layer driven only by sidewall heat flow (see also text).

The results of the last model calculation displayed in Fig. 15 are shown by the dotted line. This model calculation displays the results of a calculation using exactly the same model as that given by the continuous line, except that now there is no sidewall inflow of heat, i.e. we analytically employ a state of perfect sidewall and bottom insulation. Once again, we do not show the result of the analog equilibrium and disequilibrium calculations separately because the variation of the Rayleigh number is not significantly different. Only at times greater than 12 h, when convection is non-turbulent ($Ra < 2 \times 10^5$), is the Rayleigh number for the equilibrium model larger. In the perfectly insulated system cooled only from above convection leaves the soft turbulence regime ($Ra > 2 \times 10^5$) after about 9 h and drops below $Ra = 9 \times 10^4$ after 10 h, which marks the onset of oscillatory convection (Heslot *et al.*, 1987). The Rayleigh number decreases further and convection shuts down after about 12–13 h, when the superheat is finally gone, and about half (disequilibrium model) to one-third (equilibrium model) of the tank is still liquid. The comparison of these two model calculations (see continuous and dotted lines in Fig. 15) probably best demonstrates the impact of sidewall heating.

It is clear from this consideration that any Rayleigh number based on a length scale of 7–10 cm and, say, a ΔT of 0·1°C, which seems reasonably small without a detailed knowledge of the system, leads to the questionable conclusion that convection must be turbulent (i.e. $Ra \sim 10^6$). This example demonstrates the difficulty hidden in a simple, but at a first glance reasonable, estimate of the Rayleigh number during solidification of a multicomponent liquid. It shows that detailed analysis of various aspects of solidification (i.e. crystal growth rates, phase relations, undercoolings, etc., which we further comment on below) must be carried out before a meaningful estimate of the Rayleigh number and the dynamics of the system during solidification can be made.

DISCUSSION

Magmas are exceptionally remote and inaccessible to direct experimentation, and only very limited information is available by which to infer their dynamic evolution. Inferences drawn from laboratory analogs are thus particularly valuable in understanding magma. But these analogs, such as the present experiments represent, must be examined and understood in the broader context of other possible analogs in terms of the essential dynamic features of each system. We begin by describing the evolution of the present system and compare our interpretations and conclusions with those of Kerr *et al.* (1990*a*, 1990*b*). We then briefly compare the isopropanol system with the crystallization of paraffins and salt solutions, the last of which show internal crystallization, and then discriminate these systems from convection of fluids whose viscosity varies strongly with temperature. We close this section with a discussion of the convective velocities and with a comparison of all these analogs with the evolution of magma itself.

The isopropanol–water system

Beginning from an initial state of superheat, turbulent convection sets in almost immediately upon initiation of cooling, removing the superheat in a relatively short time (~10 h). As the superheat is lost convection wanes but is still in the soft turbulent regime, and once the superheat is gone the temperature of the bulk fluid closely tracks the liquidus temperature (see Fig. 3). The bulk fluid becomes isothermal at the liquidus temperature, showing no tendency for thermal stratification. The composition of the bulk fluid remains constant throughout the experiment. We attribute all the remaining, post superheat convective motion to sidewall heating from imperfect insulation and not from crystallization at the roof. Two lines of evidence suggest this:

(1) the detailed analytical model shows that equilibrium and disequilibrium crystallization explain the experimental results equally well (see Fig. 14). Once the superheat has been removed they both indicate a Rayleigh number of about 10^6, which can be well explained through convection driven by sidewall heating (see Fig. 15).

(2) The constant composition and temperature of the bulk fluid reveals the absence of internal crystallization, confirmed by direct observation, and overall cooling. One way to sustain convection would be through systematic cooling of the bulk liquid, which is accompanied by crystallization, but that was not observed. Convection might also be expected if progressive crystallization was driven by a finite undercooling, as suggested by Kerr *et al.* (1990*a*, 1990*b*) (see below) but that was not observed either.

To test the undercooling hypothesis we have gone to some length to establish the liquidus (–6·95 ± 0·1°C, see the Appendix) because uncertainties in the liquidus and bulk fluid temperature translate directly into large uncertainties in the estimate of the governing Rayleigh number, upon which are based all inferences on the general dynamics of the system. Even with a temperature difference of 0·1°C between the liquidus and the bulk fluid, which is the uncertainty in the liquidus determination, the Rayleigh number is greater than 5×10^5 (see Table 2; H is assumed to be 10 cm, i.e. the system is half crystallized), meaning we are well into the soft, turbulent regime. Only if the temperature difference is less than ~10^{-4}°C would convection not be expected. As

we have shown in Fig. 7, the system appears to be in equilibrium or very near its equilibrium and no significant undercooling was detected.

The crucial step in our line of evidence that convection ceases in this type of system once the superheat has been removed now is based on applying the model that was found to explain the experimental results very well to a system that is perfectly insulated. It is in this type of environment that we find convection to become non-turbulent and finally to cease (see Fig. 15).

An opposite conclusion regarding the role of disequilibrium undercooling and convection during crystallization of this system was reached by Kerr *et al.* (1990*a*, 1990*b*). From their experiments with a 16·8 wt % isopropanol–water solution (their experimental setup was essentially the same as the one described in this study) they concluded that convection is always turbulent. In short, their conclusion is based on the following line of evidence. The first model developed for the crystallization of the isopropanol–water solution is based on an equilibrium crystallization model (Kerr *et al.*, 1990*a*), where the crust buffers the magma from cooling below its liquidus, which is assumed to be at –6·2°C; convection ceases once the superheat has been removed from the melt (see Kerr *et al.*, 1990*b*), a scenario also delineated by Marsh (1989) for magma. In comparing model and experimental data, Kerr *et al.* (1990*a*) found the long-term temperature in the bulk liquid (about –6·8°C, as observed in the experiments described here) to be significantly lower (~0·6–0·7°C) than that predicted by their equilibrium model based on a liquidus temperature of –6·2°C. This difference led them to include the effects of disequilibrium crystallization.

In the disequilibrium model of Kerr *et al.* (1990*b*) (which is the same as the one in this study except for the sidewall heat flow) the small temperature difference driving turbulent thermal convection is taken to be that due to kinetic undercooling driving crystallization at the inward moving mush–melt interface. This disequilibrium model matches the data observed by Kerr *et al.* (1990*a*) almost perfectly (employing $\mathscr{G} = 2{\cdot}2 \times 10^{-6}$ m/s per °C). One of the key features of the disequilibrium model is that the underlying melt becomes supersaturated, which may initiate crystallization throughout the bulk liquid, but that was not observed in the isopropanol–water experiments. Other experiments by Kerr *et al.* (1990*b*, 1990*c*) with salt solutions did show internal crystallization and the development of an accumulation of crystals on the floor (see below). This feature can only be explained by supersaturation, for only then can crystals nucleate and grow and survive in the insulated basal mush zone.

The contrasting conclusions regarding the convective state during the water–isopropanol experiments stem from two reasons: first, Kerr *et al.* used a higher liquidus temperature (–6·2 vs –6·95°C) in their model calculations; second, their model did not include the sidewall heat flow. Taken together, these two differences promote faster crust growth (neglecting the sidewall heat flow) and bring the temperature calculated for the bulk liquid into agreement with the observed temperature (disequilibrium model calculations utilizing a liquidus temperature of –6·2°C). The different interpretations of this experiment clearly underline the importance of a proper knowledge of the phase diagram in predicting the dynamic behavior of the system.

Paraffins and salt solutions: nucleation and basal crystallization

Crystallization of paraffins

The very same behavior as found in the present experiments is found in paraffins [Viskanta, 1982 (cylindrical solidification); Brandeis & Marsh, 1989, 1990 (roofward solidification)]. Beginning with a superheated melt, vigorous thermal convection rapidly reduces the temperature to the liquidus. Early large-amplitude fluctuations in temperature systematically dampen with approach to the liquidus. Once the superheat is gone, the bulk fluid temperature remains everywhere at the liquidus until the solidification front arrives.

The phase equilibria and crystal size differ greatly in these systems. Long-chain mixed paraffins form binary solid solutions, showing no eutectic, and crystallize fully over a temperature interval of only a few degrees. Although the style of crystallization is broadly dendritic in all these systems, crystal size is very small and hair-like in the paraffins, whereas it is coarsely dendritic in ices. But what does closely link these systems is that they are all characterized by large values of the Stefan number, measured by the latent heat of fusion relative to the enthalpy associated with only the superheat (Viskanta, 1982). Convection is very effective in removing the superheat and erasing the temperature difference between the liquidus and the bulk fluid, whereupon convection ceases (Brandeis & Marsh, 1989).

Internal crystallization in salt solutions

Cooling a sodium sulfate solution, Kerr *et al.* (1990*b*, 1990*c*) observed crystals growing at the bottom of the tank even though cooling was only from above. According to those workers, these crystals nucleated either in the bulk liquid and settled or they dislodged from the upper solidification front and fell to the bottom. That the crystals did not dissolve but continued to grow is taken as evidence of sub-liquidus temperatures, i.e. undercooling in the bulk liquid. The release of light fluid from crystallization in this bottom layer drives compositional convection in the overlying fluid and steadily changes the bulk fluid

composition, lowering its liquidus. In this regard, this experiment can be compared with a liquidus determination experiment (see above) where the fluid is kept stirred by compositional convection associated with crystallization. The large release of light fluid has also been observed in NH_4Cl systems (e.g. Jahrling, 1997) and may be characteristic of salt solutions, for in paraffins, which have tiny crystals, even on cooling from below, the light rejected fluid does not rise but always stays within the solidification front (Brandeis & Marsh, 1990). In addition, Huppert & Hallworth (1993) observed the extinction of chimneys, through which most of the light fluid is released, during the bottom crystallization of salt solutions, as a result of small amounts of contamination.

Importance of analog experiments

The contradictory findings of these different studies (water–isopropanol, salt solutions, paraffins) suggest that chemically different systems behave dynamically differently when cooled from above, making it difficult to generalize results on crystallization and convection, which has been emphasized by Bennon & Incropera (1987) and demonstrated in numerical experiments by Oldenburg & Spera (1992). It appears that the dynamics of the system are intimately tied to the phase relation and kinetics, which control the network of growing crystals and the melt transport therein; the ability to nucleate and grow crystals at certain undercoolings; and the density of the residual liquid and the mush and slurry. Contamination seems also to play a major role (Huppert & Hallworth, 1993).

The interplay of all these variables is highly system dependent. The major difficulty is hidden in the fact that once phase changes are taken into account, maintaining dynamic similarity between systems becomes very difficult (F. Spera, personal communication, 1998). Even if the equilibrium phase diagram is well known, the details of kinetics add more difficulty to the problem, with the chemical field being phase lagged behind the thermal field (a disequilibrium situation). The amplitude of the phase lag is controlled by the kinetics and the associated undercooling, and therefore by the rate of cooling. However, as the thermal and chemical field both control buoyancy in the system, dynamics may be directly tied to the kinetics of nucleation and crystal growth.

How large the phase lag between thermal and chemical field is in geologically interesting systems is difficult to address, as the kinetics of nucleation and crystal growth for common minerals in a magma are rather unconstrained. In a recent study, Cashman (1993) discussed crystal growth rates as a function of cooling rate, with the growth rate decreasing with decreasing cooling rate. Therefore the phase lag and its impact on dynamics should be important in small intrusions, but larger intrusions should be less affected by the feedback between kinetics and dynamics. The importance of analog experiments is that they help understand carefully considered endmember cases. Each set of experiments (see above) looks at different aspects of multiphase crystallization processes; the water–isopropanol system specifically focuses on the effect of thermal convection in systems cooled from above excluding chemical convection. The results of those well-studied endmember cases can then be used to benchmark complex numerical models; this helps in exploring ranges of variables which are out of reach in the laboratory.

Variable viscosity effects without crystallization

Fluids whose viscosity varies strongly with temperature, but are free of crystallization, act as sluggish, perpetually superheated fluids. When cooled from above, they begin convecting slowly and increase in vigor with time. Temperature steadily falls in the bulk fluid, as it does for uniform viscosity fluids cooled from above, but no thermal plateau is encountered (e.g. Smith, 1988; Davaille & Jaupart, 1993*a*). Convection commences slowly because the high-viscosity cool lid initially advances too fast to allow instabilities to develop. Fluctuations in temperature are thus initially small, unlike for superheated crystallizing solutions, and become larger with time (Davaille & Jaupart, 1993*a*). The lack of crystallization, which makes these fluids perpetually superheated and gives them a Stefan number equal to zero, clearly sets them apart from all large Stefan number crystallizing fluids.

Measured convective velocities and calculated Rayleigh numbers

In Fig. 15 we presented the variation of the Rayleigh number with time during the experiment derived from the model calculations. Extracting the Rayleigh number from the velocity measurements described above requires the knowledge of an empirical relationship between the velocity of the bulk fluid and Ra. As the model calculations indicate a transition from hard to soft turbulence, an estimate of the Rayleigh number from velocity measurements may not be straightforward because the transition from hard to soft turbulence shows crossovers in the scaling relationships for velocity and heat flow.

We found the mean convective velocities during the experiment to decrease over the first 10 h by a factor of about 20 (see above). Visual observation of the flow pattern over the entire experiment revealed smaller eddies in the beginning, and after 9·5 h the flow was dominated by one or two large rolls and appeared to be driven

mainly by sidewall heating, which is consistent with the calculations presented above. The observation of decreasing velocity is consistent with the observations of flow during downward solidification of paraffin (Brandeis & Marsh, 1989, 1990), where plume-driven turbulent convection was described to cease once the superheat is removed. Because of easier access to the system, Brandeis & Marsh (1990) were able to measure convective velocities more frequently, the highest velocities of 6·5 ± 0·1 mm/s being found after 20 min. After about 200 min the superheat is gone and the velocity has decreased by a factor of 20. The general feature of diminishing convection upon loss of superheat seems widely appreciated in metallurgy (e.g. Flemmings, 1974, p. 228; Clyne, 1982) and in engineering studies in general (e.g. Viskanta, 1982, 1983), but there has apparently been little attempt to document this phenomenon in any detail (R. Viskanta, personal communication to B. Marsh, 1990).

Models of finite amplitude convection at large Rayleigh numbers (i.e. $Ra \gg Ra_{crit}$) suggest that convective velocity is proportional to $Ra^{2/3}$, whereas Kraichnan (1962) in his theoretical study based on a mixing length analysis found the velocity to be proportional to $Ra^{4/9}$. Direct measurements of the vertical velocity by Garon & Goldstein (1973) seem to support the exponent of 4/9. This exponent is based on data covering Rayleigh numbers from 10^5 to 5×10^9, i.e. soft and hard turbulence. They were measured by Garon & Goldstein (1973) or by others and seem to be represented fairly well by (Garon & Goldstein, 1973)

$$Ra \approx \left(\frac{WH}{0{\cdot}3871\, \kappa\, Pr^{1/3}} \right)^{9/4} = 8{\cdot}46 \times (WH)^{9/4} \kappa^{-3/2}\, \nu^{-3/4} \tag{30}$$

where the constant in the denominator has been extrapolated from fig. 10 of Garon & Goldstein (1973). W is the vertical r.m.s. velocity in the center of the system, Pr is the Prandtl number, κ is thermal diffusivity, and H is the height of the layer subject to the temperature difference ΔT.

There are two principal differences between the present experiments and the experiments that led Garon & Goldstein (1973) to relation (30): (1) their system was heated from below and cooled from above to maintain a constant temperature gradient, whereas our system is mainly cooled from above and heated slightly from the sides and below, and the temperature gradient is not fixed but steadily decreases. Therefore our system has only one conductive boundary layer extracting heat from the system. (2) Garon & Goldstein measured the variation of the velocity in a small volume in the center of the tank as a function of time and determined mean and r.m.s. velocities at a single point, whereas we only have one snapshot in time and calculate mean velocities for the whole tank at that time.

Because of these differences an estimate of the absolute values of Ra from our velocity measurements using (30) seems rather difficult and we only estimate by how many orders of magnitude Ra decreases based on our velocity measurements. Taking into account that the thickness of the fluid layer decreases about 10 cm as a result of solidification in the first 10 h, we find from (30) that Ra should decrease by about a factor of 4000 using our observed 20-fold decrease in convective velocities. This decrease in Ra indicates that the driving temperature difference, which was initially 20°C, decreases to 0·04°C after 10 h. This suggests that measuring bulk fluid velocities may be more sensitive for determining driving temperature differences than the direct measurements of minute ΔTs. However, this requires very detailed experiments to calibrate the velocity Rayleigh number relationship. Furthermore, these types of measurements will be extremely difficult, as this study has shown that small sidewall heat flows can generate turbulent convection inside the tank.

Magmatic systems

The two properties that most characterize silicate magmas are that they crystallize over a range of temperatures (e.g. 1000–1200°C) and they are not superheated; magmas are always permeated with nuclei and the governing Stefan number (based on superheat) is large. Sheet-like intrusions, where their lateral boundaries can be considered insulating, are cooled strongly from both above and below. Magmas are typically multiply saturated, crystallizing two or three phases simultaneously. Crystals grown within the solidification fronts are generally small (most often much smaller than 1 cm; e.g. Cashman & Marsh, 1988; Marsh, 1988), almost regardless of body size, and, although rarely dendritic in the usual sense, crystals commonly nucleate and grow on one another to form strings, clusters, and ganglia even at small overall crystallinities (Marsh, 1996). Comparing crystal growth rates estimated from crystal size distribution studies (e.g. Cashman, 1993) with crystal growth rates measured in the laboratory, one can estimate that the kinetic undercooling driving crystal growth is small (probably of the order of 1°C or less). It is also true that magmas are fluids whose viscosity varies enormously with increasing crystallinity and silica content, both of which are related to falling temperature.

The great challenge in understanding magma is that none of the above analog systems exactly describes magma, and that no data exist on the real-time thermal and compositional evolution of the bulk interior fluid of true subterranean magma. The phase relations of magma

are mostly well known, but no liquidus or solidus is known to better than perhaps 5–10°C. Magmas are generally not found superheated, but are commonly found at near-liquidus temperatures carrying small amounts of crystals. If there is no convection without superheat in magma, wholesale progressive cooling, crystallization, and any significant variation in composition will be absent in the deep interior. Lack of knowledge of the three-dimensional geometry of silicate nucleation and growth at small crystallinities in natural systems, however, presents a gap in simply assuming the convective histories of the binary analogs to hold also for magmas. The answer to the dynamics of the system may therefore well be hidden in the phase diagram, which controls when, at what rate, and which minerals precipitate from the melt, thereby controlling melt density and crystallinity. Whether one invokes the paraffin and water–isopropanol analog, with no internal crystallization, or the salt solution analog, with strong compositional convection driven by heavy basal crystallization, presupposes from the start the entire magmatic evolution.

Attempts to bridge this gap depend critically on how closely one applies the features of these analog systems to magma. There are four competing models:

(1) Impressed with the success of the disequilibrium model in the isopropanol analog and basal crystallization in the salt solution analog, Huppert & Worster (1992) and Worster *et al.* (1993) invoked a hybrid model of turbulent thermal convection and internal crystallization (with subsequent crystal settling).

(2) Impressed that silicate crystallization may not be dendritic, Davaille & Jaupart (1993*a*, 1994) invoked a model of variable viscosity convection; the leading edge of the solidification front was assumed to be a slurry that becomes unstable and eventually initiates convection.

(3) Beginning with a superheated magma whose phase equilibria are described by a binary eutectic, the history of convection and composition in response to simultaneous roof and wall crystallization is computed from the fully coupled set of general conservation equations based on analog systems (Oldenburg & Spera, 1992; Spera *et al.*, 1995).

(4) Impressed by the absence of superheat in magmas, the adherence of lava lakes to near-liquidus temperatures for long times, and the uniform composition of many sheet-like bodies, Marsh (1989, 1996) advocated the more or less strict paraffin or water–isopropanol analog, assuming mainly conductive heat transfer with convection only caused by initial crystal sedimentation. There is neither composition nor temperature change in the bulk magma until arrival of the solidification front.

There are problems with each of these approaches:

(1) Model (1), which is by far the most versatile and insightful analytical formulation, is based on a significant undercooling as a result of disequilibrium that is unlikely to exist in both non-superheated analogs and magmas. Assuming strong thermal convection, all results show significant cooling and compositional change in the bulk magma with time. Crust growth and internal crystallization are based purely on crystal growth without nucleation, when in fact crystallization is governed by both nucleation and growth (Kirkpatrick, 1976; Brandeis & Jaupart, 1986).

(2) Model (2) does not include crystallization and is perpetually superheated, unlike magma; magmatic crystallization may in fact have a network structure even at very small crystallinities (see Marsh, 1996; Philpotts & Carroll, 1996), which stabilizes the leading edge of the solidification front and compromises this approach.

(3) In sheet-like systems considered in this study the flow is mainly driven by cooling from the top. The fundamental physics linking convection, crystallization, and composition is not well known in magmatic and analog systems, and one needs to specify conditions dividing the mush zone into an outer viscous suspension zone and an inner porous Darcian zone. The specifics of this transition have been found to be very important for the overall dynamics of the system (e.g. Barboza & Bergantz, 1998).

(4) How closely the long-term thermal state of magma adheres to the liquidus is not known. A slow steady fall in interior temperature would point to some role for thermal convection and internal crystallization, which would point towards chemical convection.

The best set of thermal data by which to judge these models comes from Hawaiian lava lakes (15–100 m thick), and the best chemical data come from post-mortem studies of large sheet-like bodies emplaced carrying few phenocrystic crystals (see Fig. 16 and section on Geological evidence and laboratory experiments). The Hawaiian data also include information on the growth rate of the upper solidification front or crust and temperatures within the front, but no data exist for temperature measurements deep in the lakes themselves. Just as in the isopropanol experiments, however, the growth of the crust can be fitted equally well by purely conductive thermal models (Peck *et al.*, 1977; Marsh, 1989; Hort, 1997) and models assuming disequilibrium crystallization and turbulent thermal convection (Huppert & Worster, 1992; Worster *et al.*, 1993; Hort, 1997). Moreover, if nucleation is added to any of the later models of crust growth, which none of them now contain, crystal growth rate will be significantly reduced (to maintain the right thickening rate), such that the disequilibrium undercooling must also be reduced; this lessens the driving force in convection models. The thickening with time of the crust of Hawaiian lava lakes is permissive information; any number of extreme models fit within the uncertainty of the data (Hort, 1997).

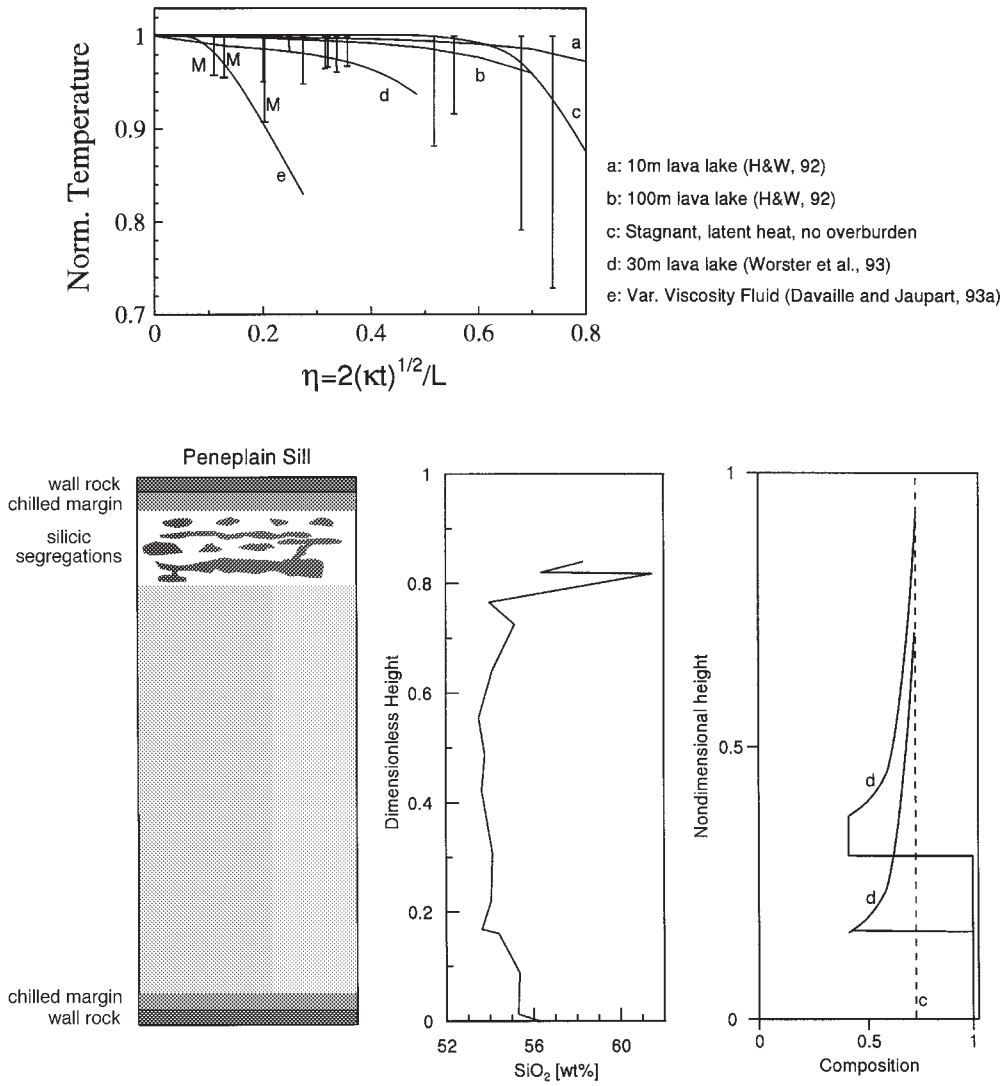

Fig. 16. The upper diagram shows a qualitative comparison of the evolution of the central temperature of a body exclusively cooled from the top. The temperature data for Makaopuhi and Alae lava lakes have been estimated from Wright & Okamura (1977) (their table 26) and Peck (1978) (his table 3) following a suggestion of Marsh (1989). There are three data points from the cooling of Makaopuhi lava lake, which have been labeled M. The data from Alae lava lake have not been labeled, for clarity in this figure. The continuous lines a and b in (a) have been taken from Huppert & Worster (1992) (H & W, 92; their fig. 18), line c from Marsh (1989) (his fig. 17), and line d from Worster *et al.* (1993) (their fig. 6; this calculation also includes cooling from below; $\kappa = 8 \times 10^{-7}$ m^2/s and a thickness of 30 m have been used). Line e is taken from Davaille & Jaupart (1993*a*) (their fig. 3). To calculate the dimensionless time a thickness of 20 cm and a $\kappa = 1{\cdot}21 \times 10^{-7}$ m^2/s has been used. In the lower part we compare the differentiation trends observed in the Peneplain Sill, Antarctica, with the general differentiation trends found in the model calculations displayed in (a). It is of importance to note that the differentiation trends resulting from the model calculation displayed as line d in (a) are dependent on the thickness of the lava lake. The two models shown qualitatively show the trends observed in a 10 m (lower curve labeled d) and 100 m (upper curve labeled d) lava lake.

This may also be true for the temperature data. The variation in bulk fluid temperature for some of the above models is compared with the lava lake temperatures in Fig. 16 [see Marsh (1989) and Hort (1997) for discussion on how the temperature data for Makaopuhi and Alae lava lake have been constructed]. We hasten to add that this comparison is not entirely fair on all counts, because none of the analog systems used in the model calculations represents true magma. Each of these systems, none the less, seeks to represent magma and does claim to predict the cooling of lava lakes, except model (e) in Fig. 16, which does not include crystallization and therefore has boundless superheat and never reaches the plateau stage shown in, for example, Fig. 3. Other than for model (e), which shows a somewhat faster cooling than observed, all models in Fig. 16a predict the temperatures observed

in the two different lava lakes fairly well. From these data one is therefore again unable to determine if the stagnant cooling model or the turbulent convection model explains the cooling of the lava lakes better.

The vertical variation in composition through solidified bodies, both actual and model, may be more diagnostic. Models (c) and (d) predict the final composition and they are compared with the composition through the 400 m thick Peneplain Sill of Antarctica in Fig. 16 [see section 2 of Marsh (1996)]. The variation in composition near the top of the Peneplain Sill is due to tearing and local segregation of melt within the upper solidification front, which is a common, but distinctly separate process in sills. Overall the composition is almost uniform through the center and lower part of the sill.

The composition predicted by model (d) shows a great deal more variation, and does not correspond particularly closely to that of the Peneplain Sill. The model (d) results do, however, broadly resemble the composition of sills that are emplaced carrying large concentrations of crystals (i.e. phenocrysts). These sills undergo extensive crystal settling immediately upon emplacement and show S-shaped composition profiles. Although model (d) does not explicitly include a physical model for crystal settling during growth, it does assume that all crystals formed in the interior, regardless of size, settle to the floor. In this regard, this model closely mimics phenocryst-laden sills; but this assumption is essential to this model in order to sustain crystallization and thermal convection. Model (c) involves crystallization only within the solidification fronts with no crystallization in the bulk fluid; the bulk composition thus remains constant, which fits the observed data more closely, but not exactly. However, a similar profile can also be generated with internal crystallization and no crystal settling.

It is of some interest to note that none of the models actually predicts the general differentiation trends described by Jaupart & Tait (1995). Their observation was that with increasing dike thickness the most differentiated liquids appear in the upper one-sixth of the magmatic intrusion. This suggests that most of the solidification took place from the bottom upwards. However, in the examples given [see figs 1 and 2 of Jaupart & Tait (1995)] the role of phenocrysts during the solidification process remains unclear. In this context it is important to note that the magma of the Peneplain Sill (see Fig. 16) was intruded phenocryst free and this sill does not show the characteristic one-sixth enrichment.

CONCLUSIONS

We have experimentally examined some aspects of the crystallization of isopropanol–water first investigated by Kerr *et al.* (1990*a*, 1990*b*), but have come to different conclusions regarding the dynamics of this system during solidification. We have also employed a theoretical model to analyze our set of experiments:

(1) the theoretical model, with the addition of sidewall heat leakage, matches the results almost perfectly; this is a versatile, flexible, and robust theoretical approach.

(2) The composition of the bulk fluid remains constant throughout the crystallization until arrival of the mush front.

(3) Lateral heat gains through imperfect insulation have a significant effect on mush growth and bulk fluid temperature, and it drives a residual Ra $\sim 10^6$ convective flow and is not related to crystallization.

(4) With perfect sidewall insulation, convection ceases in this system, as also in the paraffin system, once the superheat in gone, which occurs relatively early in the experiment.

(5) There is no significant undercooling associated with crystallization in this system; equilibrium and disequilibrium models explain the long-term evolution of bulk fluid temperature and crust thickness equally well. The absence of long-term convection precludes on more general grounds a role for undercooling in sustaining turbulent convection in this system.

(6) Although basal crystallization and compositional convection is observed in the salt solution systems, it is not seen in the present system nor is it seen in paraffin; even in basal cooling and crystallization of paraffin there in no compositional convection.

There is no obvious reason to assume that salt solutions are better analogs for magma than is a water–isopropanol solution or paraffin, which has a crystal size much more similar to that of magma. Each system has its merits and may be applicable to certain cases but no experimental system allows general conclusions. From the results presented here it appears to be untenable to generally base a Rayleigh number for magmatic convection on the undercooling associated with disequilibrium during crystallization. The dynamics of the system seem to be controlled by the phase relations, the kinetics of nucleation and growth, and the phases crystallizing.

ACKNOWLEDGEMENTS

We would like to thank O. M. Phillips for critically reading the manuscript and for helpful discussion and comments. Careful, penetrating, and insightful reviews by R. Breidenthal, P. Lowell, and F. Spera as well as anonymous referees have significantly improved the manuscript. M.H. appreciates an extensive discussion with M. G. Worster on crystallization in binary systems. Furthermore, M. G. Worster provided some numerical results to benchmark our numerical model. This work

was supported by a grant from Deutsche Forschungsgemeinschaft (Ho 1411 2-1) and by grants from the National Science Foundation (DPP-91-17576 and OPP 9418513) and the Nuclear Regulatory Commission (NRC-04-91-101) to the Johns Hopkins University.

REFERENCES

Abegg, R. (1894). Studien über Gefrierpunkte konzentrierter Lösungen. *Zeitschrift für Physikalische Chemie* **15,** 209–261.

Barboza, S. A. & Bergantz, G. W. (1998). Rheological transitions and the progress of melting of crustal rocks. *Earth and Planetary Science Letters* **158,** 19–29.

Beckermann, C. & Viskanta, R. (1993). Mathematical modeling of transport phenomena during alloy solidification. *Applied Mechanics Reviews* **46,** 1–27.

Bennon, W. D. & Incropera, F. P. (1987). A continuum model for momentum, heat and species transport in binary solid–liquid phase change systems—II. Application to solidification in a rectangular cavity. *International Journal of Heat and Mass Transfer* **30,** 2171–2187.

Bergantz, G. W. (1992). Conjugate solidification and melting in multicomponent open and closed systems. *International Journal of Heat and Mass Transfer* **35,** 533–543.

Brandeis, G. & Jaupart, C. (1986). On the interaction between convection and crystallization in cooling magma chambers. *Earth and Planetary Science Letters* **77,** 345–361.

Brandeis, G. & Marsh, B. D. (1989). The convective liquidus in a solidifying magma chamber: a fluid dynamic investigation. *Nature* **339,** 613–616.

Brandeis, G. & Marsh, B. D. (1990). Transient magmatic convection prolonged by solidification. *Geophysical Research Letters* **17,** 1125–1128.

Cashman, K. V. (1993). Relationship between plagioclase crystallization and cooling rate in basaltic melts. *Contributions to Mineralogy and Petrology* **113,** 126–142.

Cashman, K. V. & Marsh, B. D. (1988). Crystal size distribution (CSD) in rocks and the kinetics and dynamics of crystallization II. Makaopulii Lava Lake. *Contributions to Mineralogy and Petrology* **99,** 292–305.

Clyne, T. W. (1982). The use of heat flow modeling to explore solidification phenomena. *Metallurgical Transactions B* **138,** 471–478.

Davaille, A. & Jaupart, C. (1993*a*). Thermal convection in lava lakes. *Geophysical Research Letters* **20,** 1827–1830.

Davaille, A. & Jaupart, C. (1993*b*). Transient high-Rayleigh-number thermal convection with large viscosity variations. *Journal of Fluid Mechanics* **253,** 141–166.

Davaille, A. & Jaupart, C. (1994). Onset of thermal convection in fluids with temperature-dependent viscosity: application to the oceanic mantle. *Journal of Geophysical Research* **99,** 19853–19866.

Davis, S. H. (ed.) (1992). *Interactive Dynamics of Convection and Solidification*. Dordrecht: Kluwer Academic.

Dean, J. A. (1973). *Lange's Handbook of Chemistry*. New York: McGraw–Hill.

Denton, R. A. & Wood, I. R. (1979). Turbulent convection between two horizontal plates. *International Journal of Heat and Mass Transfer* **22,** 1339–1346.

Flemmings, M. C. (1974). *Solidification*. New York: McGraw–Hill.

Garon, A. M. & Goldstein, R. J. (1973). Velocity and heat transfer measurements in thermal convection. *Physics of Fluids A* **16,** 1818–1825.

Gibb, F. G. F. (1968). Flow differentiation in the xenolithic ultrabasic dykes of the Cuillins and the Strathaird Peninsula, Isle of Skye, Scotland. *Journal of Petrology* **9,** 411–443.

Gibb, F. G. F. & Henderson, C. M. B. (1992). Convection and crystal settling in sills. *Contributions to Mineralogy and Petrology* **109,** 538–545.

Glasgow, J. A. R., Streiff, A. J. & Rossini, F. D. (1945). Determination of the purity of hydrocarbons by measurement of freezing points. *Journal of Research of the National Bureau of Standards* **35,** 355–373.

Glasgow, J. A. R., Krouskop, N. C., Beadle, J., Axilrod, G. D. & Rossini, F. D. (1948). Compounds involved in production of synthetic rubber. Determination of purity by measurement of freezing points. *Annals of Chemistry* **20,** 410–420.

Goates, J. R., Ott, J. B. & Budge, A. H. (1961). Solid–liquid phase equilibria and solid compound formation in acetonitrile–aromatic hydrocarbon systems. *Journal of Physical Chemistry* **65,** 2162–2165.

Goates, J. R., Ott, J. B. & Oyler, D. E. (1966). Intermolecular compound formation in solution of n,n-dimethylformamide with carbon tetrachloride and several related substances. *Transactions of the Faraday Society* **62,** 1511–1518.

Goates, J. R., Ott, J. B. & Reeder, J. (1973). Solid–liquid phase equilibria and solid compound formation in hexafluorobenzene + benzene, + pyridine, + furan, and + thiophene. *Journal of Chemical Thermodynamics* **5,** 135–141.

Hellawell, A., Sarazin, J. R. & Steube, R. S. (1993). Channel convection in partly solidified systems. *Philosophical Transactions of the Royal Society of London, Series A* **345,** 507–545.

Heslot, F., Castaing, B. & Libchaber, A. (1987). Transitions to turbulence in helium gas. *Physical Review A* **36,** 5870–5873.

Hort, M. (1997). Cooling and crystallization in sheet-like magma bodies revisited. *Journal of Volcanology and Geothermal Research* **76,** 297–317.

Huppert, H. E. & Hallworth, M. A. (1993). Solidification of NH_4Cl and NH_4Br from aqueous solutions contaminated by $CuSO_4$: the extinction of chimneys. *Journal of Crystal Growth* **130,** 495–506.

Huppert, H. E. & Turner, J. S. (1991). Comments on 'On convective style and vigor in sheet-like magma chambers' by Bruce D. Marsh. *Journal of Petrology* **32,** 851–854.

Huppert, H. E. & Worster, M. G. (1985). Dynamic solidification of a binary melt. *Nature* **314,** 703–707.

Huppert, H. E. & Worster, M. G. (1992). Vigorous convective motion in magma chambers and lava lakes. In: Yuen, D. A. (ed.) *Chaotic Processes in Geological Sciences*. New York: Springer Verlag, pp. 141–174.

Irvine, T. N. (1980). Magmatic density currents and cumulus processes. *American Journal of Science* **280-A,** 1–58.

Jahrling, N. K. (1997). Les couches limites convectives comme moteur de l'évolution des réservoirs magmatiques. Ph.D. Thesis, Université Paris VII–Institut de Physique du Globe de Paris.

Jaupart, C. & Tait, S. (1995). Dynamics of differentiation in magma reservoirs. *Journal of Geophysical Research* **100,** 17615–17636.

Kaye, G. W. C. & Laby, T. H. (1986). *Tables of Physical and Chemical Constants and some Mathematical Functions*. Harlow, UK: Longman.

Kerr, B. C., Woods, A. W., Worster, M. G. & Huppert, H. E. (1989). Disequilibrium and macrosegregation during solidification of a binary melt. *Nature* **340,** 357–362.

Kerr, R. C., Woods, A. W., Worster, M. G. & Huppert, H. E. (1990*a*). Solidification of an alloy cooled from above Part 1. Equilibrium growth. *Journal of Fluid Mechanics* **216,** 323–342.

Kerr, R. C., Woods, A. W., Worster, M. G. & Huppert, H. E. (1990*b*). Solidification of an alloy cooled from above Part 2. Non-equilibrium interfacial kinetics. *Journal of Fluid Mechanics* **217,** 331–348.

Kerr, R. C., Woods, A. W., Worster, M. G. & Huppert, H. E. (1990*c*). Solidification of alloy cooled from above, Part 3. Compositional stratification within the solid. *Journal of Fluid Mechanics* **218,** 337–354.

Kirkpatrick, R. J. (1976). Towards a kinetic model for the crystallization of magma bodies. *Journal of Geophysical Research* **81,** 2566–2571.

Kirkpatrick, R. J. (1981). Kinetics of crystallization of igneous rocks. *Mineralogical Society of America, Reviews in Mineralogy* **8,** 321–398.

Kraichnan, R. H. (1962). Turbulent thermal convection at arbitrary Prandtl numbers. *Physics of Fluids* **5,** 1374–1389.

Lange, N. A. (1967). *Handbook of Chemistry*. New York: McGraw–Hill.

Leal, L. G. (1980). Particle motions in a viscous fluid. *Annual Review of Fluid Dynamics* **12,** 435–476.

Lejeune, A.-M. & Richet, P. (1995). Rheology of crystal-bearing silicate melts: an experimental study at high viscosities. *Journal of Geophysical Research* **100,** 4215–4229.

Lide, E. (1992). *CRC Handbook of Chemistry and Physics*. Boca Raton, FL: CRC Press.

Long, R. R. (1976). Relation between Nusselt number and Rayleigh number in turbulent thermal convection. *Journal of Fluid Mechanics* **73,** 445–451.

Mair, B. J., Glasgow, J. A. R. & Rossini, F. D. (1941). Determination of the freezing points and amounts of impurity in hydrocarbons from freezing and melting curves. *Journal of Research of the National Bureau of Standards* **26,** 591–620.

Mangan, M. T. & Marsh, B. D. (1992). Solidification front fractionation in phenocryst-free sheet-like magma bodies. *Journal of Geology* **100,** 605–620.

Mangan, M. T., Marsh, B. D., Roelich, A. J. & Gottfried, D. (1993). Emplacement and differentiation of the York Haven diabase sheet, Pennsylvania. *Journal of Petrology* **34,** 1271–1302.

Marsh, B. D. (1981). On the crystallinity, probability of occurrence, and rheology of lava and magma. *Contributions to Mineralogy and Petrology* **78,** 85–98.

Marsh, B. D. (1988). Crystal size distribution (CSD) in rocks and the kinetics and dynamics of crystallization I. Theory. *Contributions to Mineralogy and Petrology* **99,** 277–291.

Marsh, B. D. (1989). On convective style and vigor in sheet-like magma chambers. *Journal of Petrology* **30,** 479–530.

Marsh, B. D. (1991). Reply. *Journal of Petrology* **32,** 855–860.

Marsh, B. D. (1996). Solidification fronts and magmatic evolution. *Mineralogical Magazine* **60,** 5–40.

McBirney, A. R. (1995). Mechanisms of differentiation in the Skaergaard Intrusion. *Journal of the Geological Society, London* **152,** 421–435.

Oldenburg, C. M. & Spera, F. J. (1992). Modeling transport processes in nonlinear systems: the example of solidification and convection. In: Yuen, D. A. (ed.) *Chaotic Processes in Geological Sciences*. New York: Springer Verlag, pp. 205–224.

Ott, J. B. & Goates, J. R. (1992). Temperature measurement with application to phase equilibria studies. In: Rossiter, B. W. & Baetzold, R. C. (eds) *Physical Methods of Chemistry: Determination of Thermodynamic Properties*. New York: John Wiley, pp. 451–572.

Ott, B., Goates, R. J. & Waite, B. A. (1979). (Solid + liquid) phase equilibria and solid hydrate, formation in water + methyl, + ethyl, + isopropyl, and + tertiary butyl alcohols. *Journal of Chemical Thermodynamics* **11,** 739–746.

Ott, J. B., Woodfield, B. F., Guanquan, C., Boerio-Goates, J. & Goates, J. R. (1987). (Solid + liquid) phase equilibria in acetonitrile + tetrachloromethane, + trichloromethane, + trichlorofluoromethane and + 1,1,1-trichlorotrifluoroethane. *Journal of Chemical Thermodynamics* **19,** 177.

Parsons, I. (1987). *Origins of Igneous Layering*. Dordrecht: D. Reidel.

Peck, D. L. (1978). Cooling and vesiculation of Alae lava lake, Hawaii. *US Geological Survey, Professional Paper* **935-B,** 60 pp.

Peck, D. L., Hamilton, M. S. & Shaw, H. R. (1977). Numerical analysis of lava lake cooling models: Part II, Application to Alae lava lake, Hawaii. *American Journal of Science* **277,** 415–437.

Philpotts, A. R. & Carroll, M. (1996). Physical properties of partly melted tholeiitic basalts. *Geology* **24,** 1029–1032.

Press, W. H., Teukolsky, S. A., Vetterling, W. T. & Flannery, B. P. (1992). *Numerical Recipes*. Cambridge: Cambridge University Press.

Richardson, S. H. (1979). Chemical variation induced by flow differentiation in an extensive Karroo dolerite sheet, southern Namibia. *Geochimica et Cosmochimica Acta* **43,** 1433–1441.

Richter, F. M., Natif, H. C. & Daly, S. F. (1983). Heat transfer and horizontally averaged temperature of convection with large viscosity variations. *Journal of Fluid Mechanics* **129,** 173–192.

Ross, R. G., Anderson, P. & Bäckström, G. (1978). Effects of H and D order on the thermal conductivity of ice phases. *Journal of Chemical Physics* **68,** 3967–3972.

Rosso, J. C. & Carbonnel, L. (1969). Le système eau–propanol. *Comptes Rendus de l'Académie des Sciences, Serie C* **268,** 1012–1015.

Ryan, M. P., Koyanagi, R. Y. & Fiske, R. S. (1981). Modeling the three-dimensional structure of macroscopic magma transport systems: application to Kilauea volcano, Hawaii. *Journal of Geophysical Research* **86,** 7111–7129.

Ryerson, F. J., Weed, H. C. & Piwinskii, A. J. (1988). Rheology of subliquidus magmas 1. Picritic compositions. *Journal of Geophysical Research* **93,** 3421–3436.

Schooley, J. F. (1986). *Thermometry*. Boca Raton, FL: CRC Press.

Segre, G. & Silberberg, A. (1962). Behavior of macroscopic spheres in Poiseuille flow, Part 1: Determination of local concentration by statistical analysis of particle passages through crossed light beams. *Journal of Fluid Mechanics* **14,** 115–157.

Simakin, A., Schmeling, H. & Trubitsyn, V. (1997). Convection in melts due to sedimentary crystal flux from above. *Physics of the Earth and Planetary Interiors* **102,** 185–200.

Smith, M. K. (1988). Thermal convection during the solidification of a pure liquid with variable viscosity. *Journal of Fluid Mechanics* **188,** 547–570.

Solomatov, V. S. (1995). Scaling of temperature- and stress-dependent viscosity convection. *Physics of Fluids A* **7,** 266–274.

Sorensen, H. S. & Wilson, J. R. (1995). A strontium and neodymium isotopic investigation of the Fongen–Hylligen layered intrusion, Norway. *Journal of Petrology* **36,** 161–188.

Sparks, R. S. J. & Huppert, H. E. (1987). Laboratory experiments with aqueous solutions modeling magma chamber processes. I. Discussion of their validity and geological application. In: Parsons, I. (ed.) *Origins of Igneous Layering*. Dordrecht: D. Reidel, pp. 527–538.

Spera, F. J., Oldenburg, C. M., Christensen, C. & Todesco, M. (1995). Simulations of convection with crystallization in the system $KAlSi_2O_6$–$CaMgSi_2O_6$: implications for compositionally zoned magma bodies. *American Mineralogy* **80,** 1188–1207.

Tait, S. & Jaupart, C. (1992*a*). Compositional convection in a reactive crystalline mush and melt differentiation. *Journal of Geophysical Research* **97,** 6735–6756.

Tait, S. & Jaupart, C. (1992*b*). Convection and macrosegregation in magma chambers. In: Davis, S. H., Huppert, H. E., Müller, U. & Worster, M. G. (eds) *Interactive Dynamics of Convection and Solidification*. Dordrecht: Kluwer Academic, pp. 241–260.

Tilgner, A., Belmonte, A. & Libchaber, A. (1993). Temperature and velocity profiles of turbulent convection in water. *Physics Review E* **47,** 2253–2256.

Turcotte, D. & Schubert, G. (1982). *Geodynamics*. New York: John Wiley.

Turner, J. S. (1979). *Buoyancy Effects in Fluids*. Cambridge: Cambridge University Press.

Upton, B. G. J. & Wadsworth, W. J. (1967). A complex basalt–mugearite sill in Piton des Neiges Volcano, Reunion. *American Mineralogist* **52,** 1475–1492.

Vargaftik, N. B. (1983). *Handbook of Physical Properties of Liquids and Gases.* Washington, DC: Hemisphere.

Viskanta, R. (1983). Latent heat of materials. In: Lane, G. A. (ed.) *Solar Heat Storage.* Boca Raton, FL: CRC Press, pp. 153–222.

Viskanta, R. G. C. (1982). Inward solidification of a superheated liquid in a cooled horizontal tube. *Wärm- und Stoffübertragung* **17,** 39–46.

Washburn, E. W. (1929). *International Critical Tables of Numerical Data, Physics, Chemistry and Technology.* New York: McGraw–Hill.

Weast, R. C. (1970). *CRC Handbook of Chemistry and Physics.* Boca Raton, FL: CRC Press.

Wettlaufer, J. S., Worster, M. G. & Huppert, H. E. (1997). Natural convection during solidification of an alloy from above with application to the evolution of sea ice. *Journal of Fluid Mechanics* **344,** 291–316.

Worster, M. G. (1991). Natural convection in a mushy layer. *Journal of Fluid Mechanics* **224,** 335–359.

Worster, M. G., Huppert, H. E. & Sparks, R. S. J. (1990). Convection and crystallization in magma cooled from above. *Earth and Planetary Science Letters* **101,** 78–89.

Worster, M. G., Huppert, H. E. & Sparks, R. S. J. (1993). The crystallization of lava lakes. *Journal of Geophysical Research* **98,** 15891–15901.

Wright, T. L. & Okamura, R. T. (1977). Cooling and crystallization of tholeiitic basalt, 1965 Makaopuhi lava lake, Hawaii. *US Geological Survey, Professional Paper* **1004,** 1–78.

APPENDIX: THE LIQUIDUS OF THE WATER–ISOPROPANOL SYSTEM

A graphical comparison of all available data (Abegg, 1894; Lange, 1967; Rosso & Carbonnel, 1969; Ott *et al.*, 1979) for the water-rich side of the binary water–isopropanol is shown in Fig. Al. Overall the results compare favorably with one another, but there are some systematic differences. Within the compositional range of interest (dotted vertical line in Fig. A1), Abegg's data fall about 0·7°C above the data of Ott *et al.*, whereas Lange's data fall about 1·6°C lower (uppermost diagram). The data of Rosso & Carbonnel coincide—in the region of interest—with those of Ott *et al.*, albeit with a slightly different slope (middle diagram in Fig. A1). Each data set shows some slight curvature and is fitted very well by a second-order polynomial, which are the lines actually shown through each set of points in Fig. Al. Over a still more restricted compositional range, the relative positions of the fitted curves are clearly apparent in the lowermost diagram of Fig. Al. At the exact composition of interest (i.e. X_{water} = 0·9428 or 16·8 wt % alcohol), the entire range of temperature differences between the highest (Abegg) and lowest (Lange) liquidus amounts to about 2°C. Without further information it is difficult to choose one liquidus over another, and next we examine the experimental methods used in each liquidus determination.

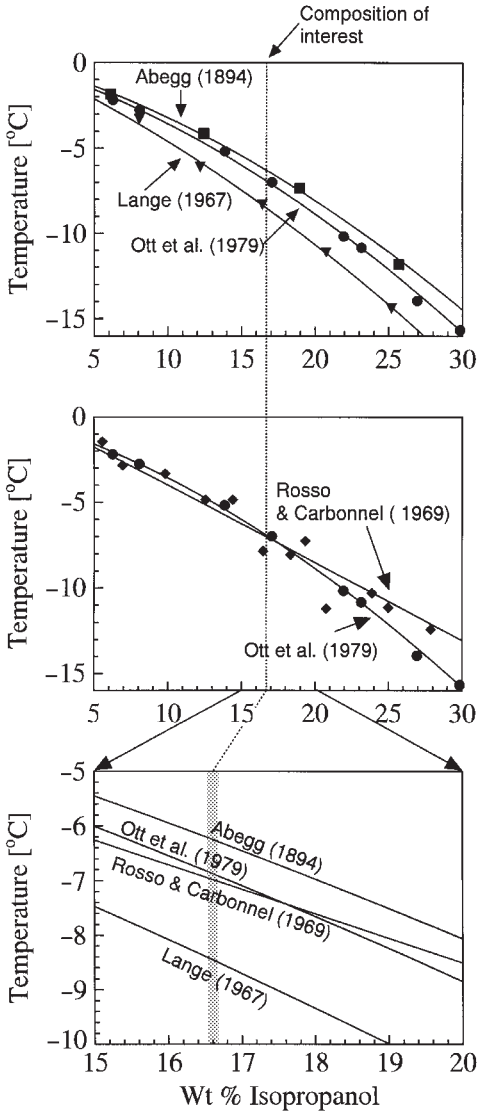

Fig. A1. Liquidus temperature of water–isopropanol mixtures as a function of the water content. The part of the phase diagram that is of specific interest to this study is shown. Here we compare the data sets of various studies. The continuous lines fitted through the data are best second-order polynomial fits for isopropanol <30 wt %.

Comparison of experimental methods

(1) Abegg (1894) used a hand-made mercury thermometer, subdivided into 1/50 degree divisions, to measure the freezing points. He calibrated the thermometer against the hydrogen thermometer, which had been established in 1887 as a standard (Schooley, 1986). He reported an uncertainty in his temperature readings for experiments on some more concentrated solutions of as high as 0·07°C to sometimes as high as 0·15°C. He also stated that the undercooling was always only a couple of

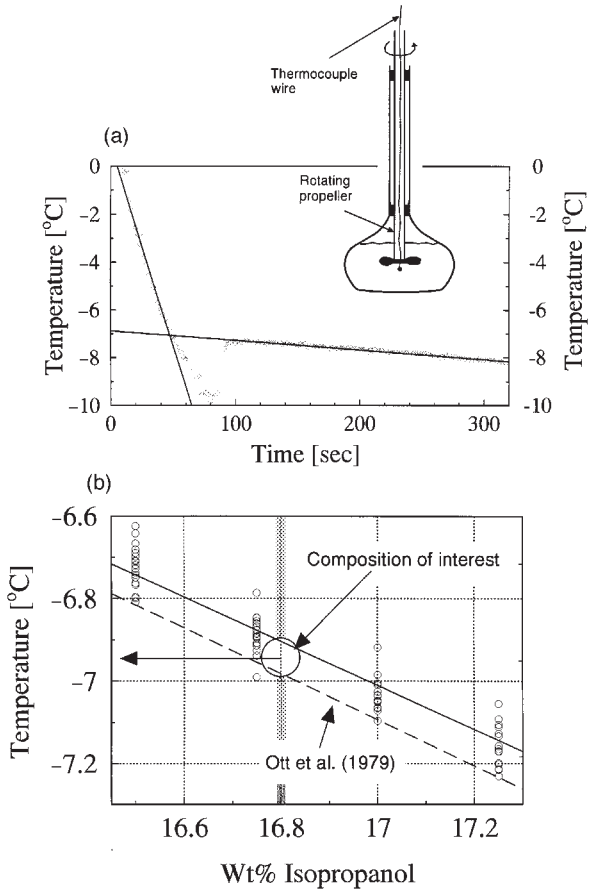

Fig. A2. (a) Temperature as a function of time in one of our liquidus measurements for a 17 wt % water–isopropanol solution and a schematic drawing of our experimental setup to determine the liquidus temperature. In all our liquidus determinations we fitted the first line through the data ranging from –1°C to –7°C and the second line through an interval of 200 s after the release of the latent heat because of the nucleation event. The R^2 values were generally >0·99. (b) Results of our 70 liquidus measurements (○), a comparison of our data with the measurements of Ott *et al.* (1979) (dashed line).

hundredths of a degree. For each composition studied, Abegg calculated a mean temperature from the three highest 'good' values, which he reported as his five liquidus temperatures. Without knowledge of his entire data set, which he did not publish, it is impossible to evaluate his data further.

(2) Lange's (1967) data are reported in the *Handbook of Chemistry* edited by N. A. Lange, which beginning in 1934 has had at least 11 editions (e.g. Dean, 1973). This compendium gives no reference to the original experiments nor does it give any information on the experimental methods or uncertainties; that the listing is headed with the title 'Freezing Point' and not 'Melting Point' may suggest something of the method.

(3) The data of Rosso & Carbonnel (1969) were obtained by differential thermal analysis (DTA). Although they did not list their original numbers (and attempts to locate them have been unsuccessful), we have digitized their data from their published phase diagram and these are the data used in Fig. Al. These data stand out in two ways. First, they have the most scatter, possessing a standard deviation of 0·87°C whereas each of the other data sets has a standard deviation of <0·26°C. Second, they display upward curvature whereas all the other data show downward curvature. Fortunately, however, this divergence becomes marked only for compositions well beyond the region of present interest.

(4) The data of Ott *et al.* (1979) were obtained using a simple but effective apparatus originally developed by the National Institute of Science and Technology (Mair *et al.*, 1941; Glasgow *et al.*, 1945, 1948). In brief, the solution is heated or cooled while its temperature is carefully monitored; for any composition, upon reaching a phase boundary the temperature becomes constant (for a pure substance) or rises (drops) slowly, for a solution, until melting (crystallization) is complete. The accuracy of the method rests essentially on the determination of temperature and on the accuracy of the solution composition. Beginning in 1960, this same apparatus, eventually with a computer, has been used by J. B. Ott and J. R. Goates and associates in a wide range of studies of phase equilibria in organic systems (e.g. Goates *et al.*, 1961, 1966, 1973; Ott *et al.*, 1979, 1987). This method of experiment as well as the measurement of temperature in such systems has been described in a comprehensive chapter by Ott & Goates (1992). Because of sluggish crystallization kinetics in the isopropanol system, Ott *et al.* (1979) used melting reactions to measure the liquidus for the entire system. They stated an uncertainty in the determined phase boundary of 0·1°C (J. B. Ott, personal communication, 1992) and an uncertainty of 0·5°C in areas of the phase diagram where hydrates or isopropanol itself is freezing.

(5) In summary, the sluggish crystallization kinetics of ice in alcohols may explain why Abegg used only his three highest 'good' temperatures to form a mean for the liquidus. This method is apt to give too high a liquidus, whereas if Lange's data are from freezing experiments without due concern for undercooling, these data are apt to underestimate the liquidus. On the other hand, that the Ott *et al.* melting experiments and the Rosso & Carbonnel DTA experiments agree so well over the compositional range of interest may reflect the abilities of these methods to circumvent this kinetic obstacle, and the liquidus temperature at 16·8 wt % isopropanol is near –7°C.

The liquidus temperature of a 16·8 wt % solution

To augment the existing liquidus determinations, we made a total of 70 liquidus determinations at four specific

compositions bracketing the composition of interest. At compositions of 16·5, 16·75, 17·0, and 17·25 wt % isopropanol, 22, 19, 14, and 15 experiments, respectively, were performed using the basic method of Ott *et al.* (1979). A 10 ml Erlenmeyer flask filled with ~8 ml of solution was submerged in a ~–12°C bath and its temperature was continuously monitored electronically with a thermocouple (see Experimental setup section). To avoid the kinetic problem of delayed crystallization or undercooling, the solution was continuously stirred, as suggested by Ott *et al.* (1979). A representative cooling history for a 17 wt % solution is shown in Fig. A2a along with a schematic drawing of the apparatus used. The actual liquidus temperature is found by fitting two straight lines to the data (see Fig. A2a), the intersection of which gives the liquidus. Under these rapid rates of cooling, even with stirring, there is still ~3°C of undercooling, but the temperature recovers rapidly in response to crystallization and the data trace is long and very well behaved; estimation of the liquidus is straightforward. The cooling history is exactly that expected for a solution, where the later sub-horizontal slope reflects the changing solution composition with progressive crystallization (Ott & Goates, 1992).

These new data place tight limits on the liquidus temperature over this restricted range of composition (see Fig. A2b). Considered alone, the full spread of the data at any of these compositions is about 0·2°C. These data are well represented by a linear fit, about which they exhibit a standard deviation of 0·046°C (see Fig. A2b). The liquidus found by Ott *et al.* (1979), which is essentially coincident with that of Rosso & Carbonnel (1969) in this region, is slightly (~0·1°C) below that defined by these new data, with a standard deviation relative to the Ott *et al.* liquidus of 0·048°C (see Fig. A2b). The uncertainty in the Ott *et al.* liquidus alone is 0·1°C, so these three data sets are fully compatible. At the composition of interest for the present experiments (16·8 wt % alcohol, $X_{water} = 0{\cdot}9428$) our best estimate of the liquidus temperature is –6·95 ($\pm$0·1)°C, which is rounded to the nearest 0·05°C.